NAVAL POSTGRADUATE SCHOOL

MONTEREY, CALIFORNIA

THESIS

TURBULENT STRUCTURE UNDER SHORT FETCH WIND WAVES

by

Michael J. Papa

December 2015

Thesis Advisor: Timothy P. Stanton
Second Reader: Timour Radko

Approved for public release; distribution is unlimited

THIS PAGE INTENTIONALLY LEFT BLANK

REPORT DOCUMENTATION PAGE		*Form Approved OMB No. 0704–0188*
Public reporting burden for this collection of information is estimated to average 1 hour per response, including the time for reviewing instruction, searching existing data sources, gathering and maintaining the data needed, and completing and reviewing the collection of information. Send comments regarding this burden estimate or any other aspect of this collection of information, including suggestions for reducing this burden, to Washington headquarters Services, Directorate for Information Operations and Reports, 1215 Jefferson Davis Highway, Suite 1204, Arlington, VA 22202-4302, and to the Office of Management and Budget, Paperwork Reduction Project (0704-0188) Washington, DC 20503.		
1. AGENCY USE ONLY (*Leave blank*)	**2. REPORT DATE** December 2015	**3. REPORT TYPE AND DATES COVERED** Master's thesis
4. TITLE AND SUBTITLE TURBULENT STRUCTURE UNDER SHORT FETCH WIND WAVES		**5. FUNDING NUMBERS**
6. AUTHOR(S) Michael J. Papa		
7. PERFORMING ORGANIZATION NAME(S) AND ADDRESS(ES) Naval Postgraduate School Monterey, CA 93943-5000		**8. PERFORMING ORGANIZATION REPORT NUMBER**
9. SPONSORING /MONITORING AGENCY NAME(S) AND ADDRESS(ES) N/A		**10. SPONSORING/MONITORING AGENCY REPORT NUMBER**
11. SUPPLEMENTARY NOTES The views expressed in this thesis are those of the author and do not reflect the official policy or position of the Department of Defense or the U.S. Government. IRB Protocol number _____N/A_____.		
12a. DISTRIBUTION/AVAILABILITY STATEMENT Approved for public release; distribution is unlimited		**12b. DISTRIBUTION CODE**
13. ABSTRACT (maximum 200 words)		

Momentum transfer from wind forcing into the ocean is complicated by the presence of surface waves. Wind momentum and energy are partitioned into wave growth, wave breaking, and wave forcing of the ocean surface layer. The purpose of this study was to support the ONR Coupled Boundary Layers and Air-Sea Transfer program by making very high spatial resolution profile measurements of the 3-D velocity field into the crest-trough region of wind-forced surface gravity waves, and study the low-frequency turbulent motions below the waves. The overarching goal is to improve model parameterization of how momentum is imparted on the ocean via wind-driven processes. At the Salinas River, in California, the Bistatic Coherent Acoustic Doppler Velocity Profiler and Thies Clima Ultrasonic 3-D Anemometer were deployed to capture the above-surface and subsurface velocity fields simultaneously to explore three main objectives: 1) determine the wave energy decay with depth and confirm the wavenumber, 2) determine the observed wind stress and calculate the wind stress using a bulk formula to identify any variations as a result of this estuarine environment, and 3) determine the turbulent stresses in the water column below the waves, and confirm the presence of Langmuir circulations and determine their advection and scaling.

14. SUBJECT TERMS Langmuir circulation, Bistatic Coherent Acoustic Doppler Velocity Profiler, surface gravity wave turbulence, Coupled Boundary Layers and Air-Sea Transfer, wind stress			**15. NUMBER OF PAGES** 77
			16. PRICE CODE
17. SECURITY CLASSIFICATION OF REPORT Unclassified	**18. SECURITY CLASSIFICATION OF THIS PAGE** Unclassified	**19. SECURITY CLASSIFICATION OF ABSTRACT** Unclassified	**20. LIMITATION OF ABSTRACT** UU

THIS PAGE INTENTIONALLY LEFT BLANK

TURBULENT STRUCTURE UNDER SHORT FETCH WIND WAVES

Michael J. Papa
Lieutenant Commander, United States Navy
B.S., United States Naval Academy, 2005

Submitted in partial fulfillment of the
requirements for the degree of

**MASTER OF SCIENCE IN METEOROLOGY AND PHYSICAL
OCEANOGRAPHY**

from the

**NAVAL POSTGRADUATE SCHOOL
December 2015**

Approved by: Timothy P. Stanton
Thesis Advisor

Timour Radko
Second Reader

Peter C. Chu
Chair, Department of Oceanography

THIS PAGE INTENTIONALLY LEFT BLANK

ABSTRACT

Momentum transfer from wind forcing into the ocean is complicated by the presence of surface waves. Wind momentum and energy are partitioned into wave growth, wave breaking, and wave forcing of the ocean surface layer. The purpose of this study was to support the ONR Coupled Boundary Layers and Air-Sea Transfer program by making very high spatial resolution profile measurements of the 3-D velocity field into the crest-trough region of wind-forced surface gravity waves, and study the low-frequency turbulent motions below the waves. The overarching goal is to improve model parameterization of how momentum is imparted on the ocean via wind-driven processes. At the Salinas River, in California, the Bistatic Coherent Acoustic Doppler Velocity Profiler and Thies Clima Ultrasonic 3-D Anemometer were deployed to capture the above-surface and subsurface velocity fields simultaneously to explore three main objectives: 1) determine the wave energy decay with depth and confirm the wavenumber, 2) determine the observed wind stress and calculate the wind stress using a bulk formula to identify any variations as a result of this estuarine environment, and 3) determine the turbulent stresses in the water column below the waves, and confirm the presence of Langmuir circulations and determine their advection and scaling.

THIS PAGE INTENTIONALLY LEFT BLANK

TABLE OF CONTENTS

THIS PAGE INTENTIONALLY LEFT BLANK

LIST OF FIGURES

THIS PAGE INTENTIONALLY LEFT BLANK

LIST OF ACRONYMS AND ABBREVIATIONS

3-D	three dimensional
ABL	atmospheric boundary layer
ASIT	Air-Sea Interactions Tower
BCDVP	Bistatic Coherent Acoustic Doppler Velocity Profiler
BLT	boundary layer turbulence
CBL	coupled boundary layer
CBLAST	Coupled Boundary Layers and Air-Sea Transfer
CBLAST-LOW	Coupled Boundary Layers and Air-Sea Transfer Experiment in Low Winds
cph	cycles per hour
COAMPS	Coupled Ocean-Atmosphere Mesoscale Prediction System
DRI	Department Research Initiative
GPS	Global Positioning System
IR	infrared
LFT	linear filtration technique
LSC	Langmuir supercells
LWT	linear wave theory
MILDEX	Mixed Layer Dynamics Experiment
MVCO	Martha's Vineyard Coastal Observatory
NRL	Naval Research Laboratory
ONR	Office of Naval Research
OSBL	ocean surface boundary layer
rms	root mean squared
ROMS	Regional Ocean Modeling System
RTP	Real Time Profiler
SST	sea surface temperature
TDM	triple decomposition method
THIES	Thies Clima Ultrasonic 3-D Anemometer
VADCP	five-beam acoustic Doppler current profiler
VMCM	Vector Measuring Current Meters
WBL	wave boundary layer

THIS PAGE INTENTIONALLY LEFT BLANK

ACKNOWLEDGMENTS

THIS PAGE INTENTIONALLY LEFT BLANK

I.   INTRODUCTION

As wind blows across the ocean surface an atmospheric boundary layer forms and momentum is transferred across the air/ocean interface, forming a turbulent boundary layer in the upper ocean. Part of the momentum is passed into forming waves, while part directly forces the ocean surface. The presence of evolving waves greatly complicates our understanding of the atmosphere/ocean coupling, as the large magnitude, highly irrotational wave motions readily mask the turbulent motions that are typically one or two orders of magnitude smaller, and yet transfer the wind's momentum into the ocean interior. Turbulence has a large influence above the sea surface in the development of wind waves, while below the surface additional turbulence is caused by wave breaking and waves nonlinear interactions across varying scales. It is therefore important to not only capture the above-surface velocity fields but also those below the surface simultaneously in order to understand and model this wind/ocean momentum transfer.

The purpose of this study was to make very high spatial resolution profile measurements of the three-dimensional (3-D) velocity field right up to the crest-trough region of wind-forced surface gravity waves, and study the low frequency turbulent motions below the waves. This furthered the understanding and modeling of how momentum is imparted on the ocean via wind-driven waves.

A.   OCEAN TURBULENCE

Nearly 500 years ago, turbulence was first recognized by Leonardo da Vinci; however, it was not until the 1930s that a mathematical description of turbulence was first attempted by G. I. Taylor. Utilizing statistical correlations, Fourier transforms, and power spectra, Taylor was able to analyze homogeneous isotropic turbulence (Flierl and Ferrari 2007). The Taylor microscale (λ), or turbulent microscale, defined by

$$\left(\frac{\partial u'}{\partial x} \right)^2 = \frac{u'^2}{\lambda^2} \, , \tag{1.1}$$

1

where u' is the root mean squared (rms) of the fluctuating velocity field delineates the boundary of the inertial subrange and the start of the dissipation subrange where the fluid viscosity starts to dominate, as seen in Figure 1 (Pope 2000).

In 1941, Kolmogorov developed the K41 theory, which serves as a basis for many current theories of turbulence (Flierl and Ferrari 2007). K41 finds that despite smooth forcing and initial conditions, irregular and complex flows will develop across multiple scales within turbulent flows. In ensemble averaged velocity spectra of active turbulent boundary layers a statistical equilibrium was found where concentrated small-scale energy dissipation balanced large-scale energy inputs. Second, an energy spectrum $E(\kappa)$ is observed over a wide range of wavenumbers that satisfies the equation

$$E(\kappa) = \alpha(\epsilon)^{\frac{2}{3}} * \kappa^{-5/3} \, , \tag{1.2}$$

where $\alpha \sim 1.5$ is the empirical constant, ϵ is the energy dissipation rate and κ is the radian wavenumber

$$\kappa = 2\pi k \tag{1.3}$$

(Govender et al. 2004).

This equation for $E(\kappa)$ is valid across the inertial subrange, beyond which will display a rapid exponential decay through the dissipation range as shown in Figure 1.

There are six properties that best distinguish turbulence:

1. "Turbulence is irregular and is defined as 'An irregular condition of flow in which the various quantities show a random variation with time and space coordinates, so that statistically distinct average values can be discerned.'" (Hinze 1975)

2. "Turbulence is highly diffusive, which causes rapid mixing and increases transfer rates of momentum scalar properties within the fluid." (McPhee 2008)

3. "Turbulence occurs at high Reynolds numbers, as instabilities from interactions of viscous and inertial forces manifest themselves." (McPhee 2008) This means that ratios between the largest and smallest length scales are important in characterizing turbulence as seen in Figure 1. Well resolved turbulent spectra allow the turbulent production and dissipation scales to be identified, allowing the definition of turbulent Reynolds numbers (Flierl and Ferrari 2007). "The Reynolds number (Re) is defined as

$$Re = \frac{U*L}{\upsilon}, \tag{1.4}$$

where U is the characteristic velocity, L is the characteristic length scale in the flow, and v is the kinematic molecular viscosity." (McPhee 2008)

4. "Turbulence at high Reynolds numbers is a characteristic of the flow rather than the particular fluid." (McPhee 2008)

5. "Turbulence is essentially dissipative, meaning that work must be done to maintain viscous losses to internal energy of the flow." (McPhee 2008)

6. "Well-developed unstratified turbulence is both highly rotational and three dimensional." (McPhee 2008)

Turbulent motions are inherently unpredictable predict in space and time due to their nonlinear nature. It can only be forecasted for short periods using current fluid dynamic equations due to the strength of the nonlinearities of turbulent motions. Far from boundaries, well developed unstratified turbulence is isotropic and homogenous. Here "isotropic" means there is a statistically averaged uniform fluctuation magnitude in all directions, while "homogenous" refers to a lack of spatial gradients across any averaged quantity (Flierl and Ferrari 2007).

A key approach to analyzing turbulence is Taylor's (1938) frozen turbulence hypothesis, which relates time domain observations of turbulent motions at a fixed location to the spatial domain of the eddy field advecting past the sensor. The assumption is that the turbulent field is evolving at a timescale much longer than the advective timescale. The frozen turbulence hypothesis is complicated when establishing a relationship between turbulence in the influence of the strong, periodic, irrotational flow under surface gravity waves.

Figure 1. Energy Spectrum Breakdown and Distribution Based on the Kolmogorov Scale
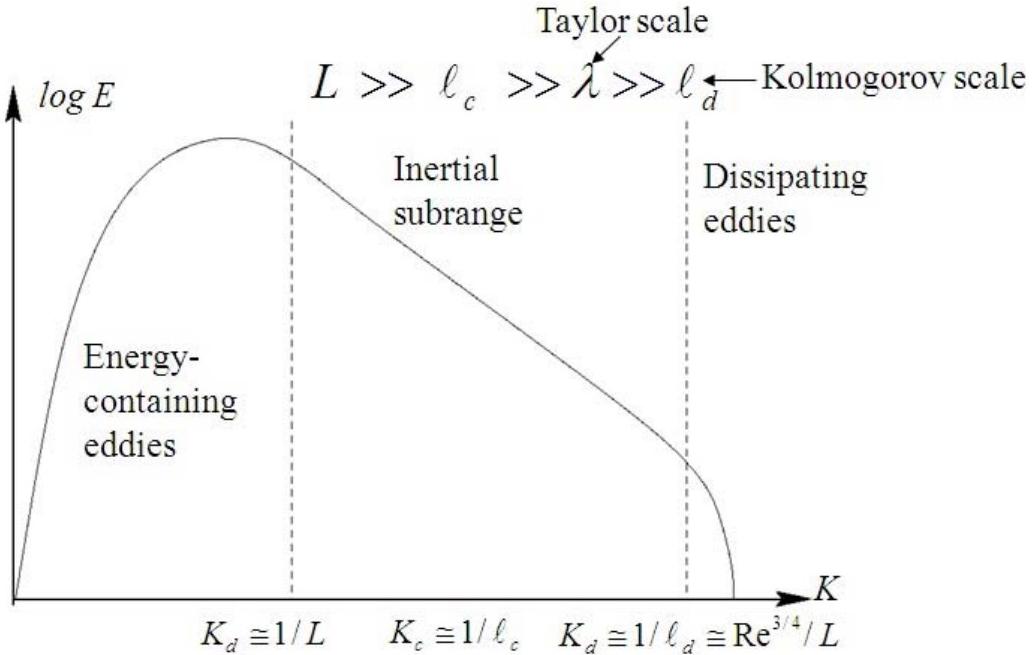
The energy containing portion of the spectrum, inertial subrange, and the dissipation portion of the spectrum are designated by region. Using eddy and turbulent length scales (L, l), these regions are separated by the cutoff wave number $(k_c) = \frac{1}{L}$, the roll off wave number (k_o), and the dissipation wave number (k_d) described as $\frac{Re^{3/4}}{L}$ with Re representing the Reynolds number. Adapted from Hossain, N., 2012: Turbulence modeling. Computational Mechanics. Accessed September 1, 2015. [Available online at: http://naimhossain.blogspot.com/2012/08/turbulence-modeling.html.]

B. FLOW UNDER SURFACE GRAVITY WAVES

Since this is a study of turbulence in the presence of surface gravity waves, it is important to review the flow field under ocean surface gravity waves. Airy theory was designed to provide a relationship between the local sea surface elevation and velocity or pressure fields under surface gravity waves. While it assumes a flat bottom, it is valid both inside and outside the surf zone (Guza and Thornton 1980). Early research, such as that conducted by Bowen in 1966 and Sampson in 1969, focused on the relationship of the mean water depth (h) and the deep-water wavelength of the spectral peak (L) to relate the sea surface elevation and velocity at a single location.

The use of linear wave theory (LWT) and the linear superposition of independent sinusoids allow an accurate equation describing the local sea surface elevation $\eta(t)$

$$\eta(t) = \sum_{n=1}^{\infty} a_n \cos\left(k_n * x + \sigma_n t + \varepsilon_n\right) = \sum_{n=1}^{\infty} \eta_n , \tag{1.5}$$

where a_n is the amplitude, x is the horizontal displacement, t is time, ε_n is the phase angle, k_n is the horizontal vector wave number, and σ_n is the frequency relation to k via linear wave theory. The relation between σ_n and k is

$$\sigma_n^2 = g|k_n| \tan|k_n| h , \tag{1.6}$$

where g is gravity and h is the total water depth (Guza and Thornton 1980). From these equations a relationship between the sea surface elevation and velocity field can be made using a spectral transfer function

$$u(t) = \sum_{n=1}^{\infty} \left[\frac{\sigma_n \cosh|k_n|(h+z)}{\sinh|k_n|h} \right] \eta_n , \tag{1.7}$$

where z is the depth of interest (Guza and Thornton 1980).

In addition to this LWT relation between η and the velocity field, researchers began to relate their findings by also using the Ursell number. The Ursell number (Ur) defines the nonlinearities associated with long period surface gravity waves via the equation

$$Ur = \frac{a}{h(kh)^2} , \tag{1.8}$$

where a is the amplitude, h is the mean water depth, and k is the wavenumber of the spectral peak. The amplitude a was derived from

$$a_{1/3} = \frac{H_s}{2} = 2\upsilon , \tag{1.9}$$

where v is the RMS value of the surface elevation. A small Ur indicates that LWT is applicable when long period waves are involved (Guza and Thornton 1980).

Linear wave theory for surface gravity waves was found to be limited values of Ur was less than 0.3 (Madsen 1971). For higher values, despite the nonlinearity present Airy wave theory remained reasonably accurate based on the results from Guza and Thornton (1980). Additionally, they found that at higher harmonics, errors in predicting

5

the velocity field became more pronounced suggesting increased nonlinearity at higher frequencies.

C.   TURBULENCE UNDER WIND-FORCED SURFACE GRAVITY WAVES

Turbulence under wind-generated waves has been studied in the lab and in the field only over the past few decades. This is a challenging observational and theoretical topic as the turbulent fluctuations are typically about two orders of magnitude smaller than the orbital wave velocity field.

During field measurements collected on Lake Ontario, the turbulent kinetic energy and dissipation rates were found to intensify with respect to the turbulent boundary flow, suggesting that shear production is not the sole generator of turbulence below wind-driven waves. Furthermore, an additional spectral bump was noted near the dominant wave frequency, which indicated that turbulent fluctuations were advected by mean current flow and orbital wave motions (Magnaudet and Thais 1995).

Figure 2.   Example Autospectra of Vertical Velocity Fluctuations
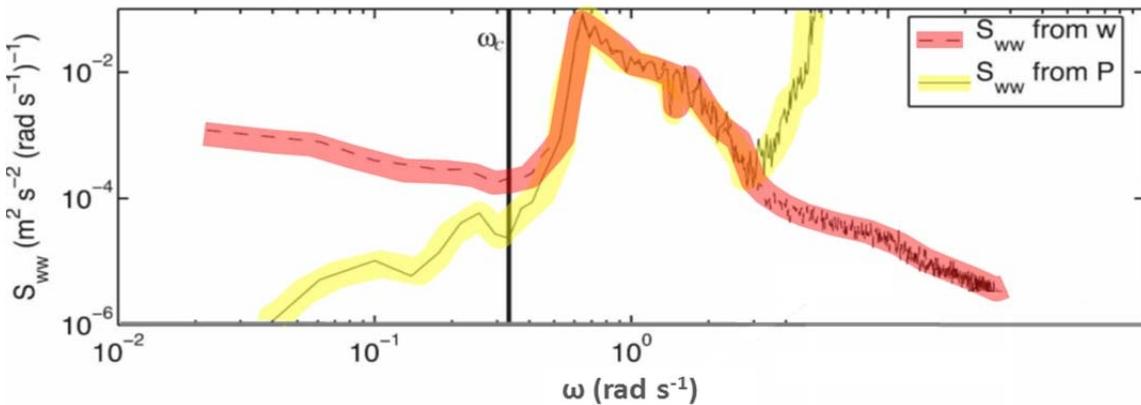
"The dashed line is the mean spectrum from the velocity records at four ADVs, and the solid line is the spectrum from a single pressure sensor and assumes a linear wave transfer function to determine the velocity spectrum (Equation 1.24). The pressure spectrum at frequencies above 2 rad s^{-1} is dominated by white noise, causing the lack of agreement between the spectra at high frequency. The frequency band in which the two spectra overlie one another is the wave band. The thick vertical line is the wave band cutoff ω_c used for separating below-wave-band (turbulence) motions from wave band motions." Source: Gerbi, G. P., J. H. Trowbridge, J. B. Edson, A. J. Plueddemann, E. A. Terray, and J. J. Fredericks, 2008: Measurements of momentum and heat transfer across the air–sea interface. *J. Phys. Oceanogr.*, **38**, 1054–1072.

Evident by the findings at Lake Ontario, turbulent energy will dominate the spectrum to the left of the wave band cutoff frequency. The breakdown of the Kolmogorov scale (Figure 1) relates to the example spectrum shown in Figure 2, where the inertial subrange is to the right of the wave band cutoff frequency and will contain both wave energy and some turbulent energy, making it difficult to isolate the turbulent contribution to the vertical velocity field. The turbulent energy containing portions of the spectrum and inertial subrange are the areas of interest for Figure 2. It is important to note that the dissipation range as described in Figure 1 is not resolved in this data.

In order to resolve the turbulent energy, the dominant wave orbital motion in the vertical velocity spectra is required to be separated from turbulent velocities. Researchers have developed a number of methods in an attempt to resolve this issue to include the triple decomposition method, frozen turbulence hypothesis, and use of the turbulence energy cospectra as function of the frequency. Further complications arise from wave-breaking events and the presence of Langmuir circulation components, which are defined in the following sections.

1. Triple Decomposition Method

Developed by Magnaudet and Thais (1995), the triple decomposition method (TDM) allows the separation of the three contributors to fluctuating motions: potential orbital motion, rotational orbital motion, and turbulent fluctuations. The method relies on an extension of the Dean (1965) method and the linear filtration technique (LFT) to perform its decomposition of the velocity field under waves.

The Dean method is used to determine the potential orbital motion by using a Fourier expansion of an analytical stream function to describe flow under a nonlinear gravity wave. More importantly, this method provides an ideal fit to surface layer boundary conditions, especially for nonlinear waves with heights greater than 50% of the breaking height. An advantage of the Dean method is that it deals with waves that "include a uniform steady current and specified pressure distribution across the free surface" (Dean 1965).

Benilov et al. (1970) developed the LFT utilizing the concurrent measurement of sea surface elevation (η) and the near surface velocities to isolate the wave induced motions using a linear filter. The LFT's two key assumptions were best summarized by Jiang et al. (1990): (1) there is a linear relation between wave-induced motions and water displacement, and (2) there is no correlation between wave-induced motion and turbulence. This method follows closely with Equation 1.8.

In a follow-on article, Benilov et al. (1974) identifies a key parameter for evaluating the air flow structure over the sea during various stage of wave development. Defined by

$$\frac{c_0}{u_*},$$ (1.10)

where c_o is the phase velocity of the main energy-containing component of the wave spectrum. The friction velocity (u_*) is described by the equation

$$u_* = (-\overline{u'w'})^{1/2},$$ (1.11)

where $\overline{u'w'}$ is the covariance between the horizontal and vertical velocity components. Higher values (~85) for this parameter indicate attenuated wind generated waves, while lower values (~20) indicate developing wind-generated waves.

Together the LFT and Dean method were utilized by Magnaudet and Thais (1995) to develop the TDM. The TDM uses a nonlinear method via an extension of the Dean method, to compute the velocity fluctuations that relate to the potential orbital motions by making an assumption that the motion is 2-D and nondispersive, while allowing a mean drift.

2. Frozen Turbulence Hypothesis

The previously discussed frozen turbulence hypothesis has an important role in the turbulence-wave relationship and produces the resulting wave number-frequency relation

$$\omega = kU_d,$$ (1.12)

where ω is the radian frequency, U_d is the steady drift speed, and k is the radian wavenumber described by

$$k = \frac{2\pi}{\lambda},$$
(1.13)

where λ is the turbulent length scale. The frozen turbulence hypothesis is based on steady advection in boundary layer flows, making it a crucial concept when using an Eulerian sensor (fixed in location while the environment moves around it). This scaling has to be used carefully when orbital velocities from surface waves are introduced. A much more complicated pattern of the turbulent eddies is observed from an Eulerian sensor as the turbulent eddy field is carried by wave orbital motions. As a result, the spectral energy of the turbulence field is moved upband because of the wave orbital motion (Figure 3). This is a key concept in understanding how the spectrum in Figure 2 is changed by unsteady advection. To simplify the effects of wave motion induced by unsteady advection in the frequency domain, a restriction of the horizontal motion was reduced to a single direction, x along the wave propagation direction. In part this simplification led to a more streamlined means of predicting the turbulence cospectra in the frequency domain (Gerbi et al. 2008).

Figure 3.   Unsteady Frozen Turbulence Spectrum Affected by Wave Energy
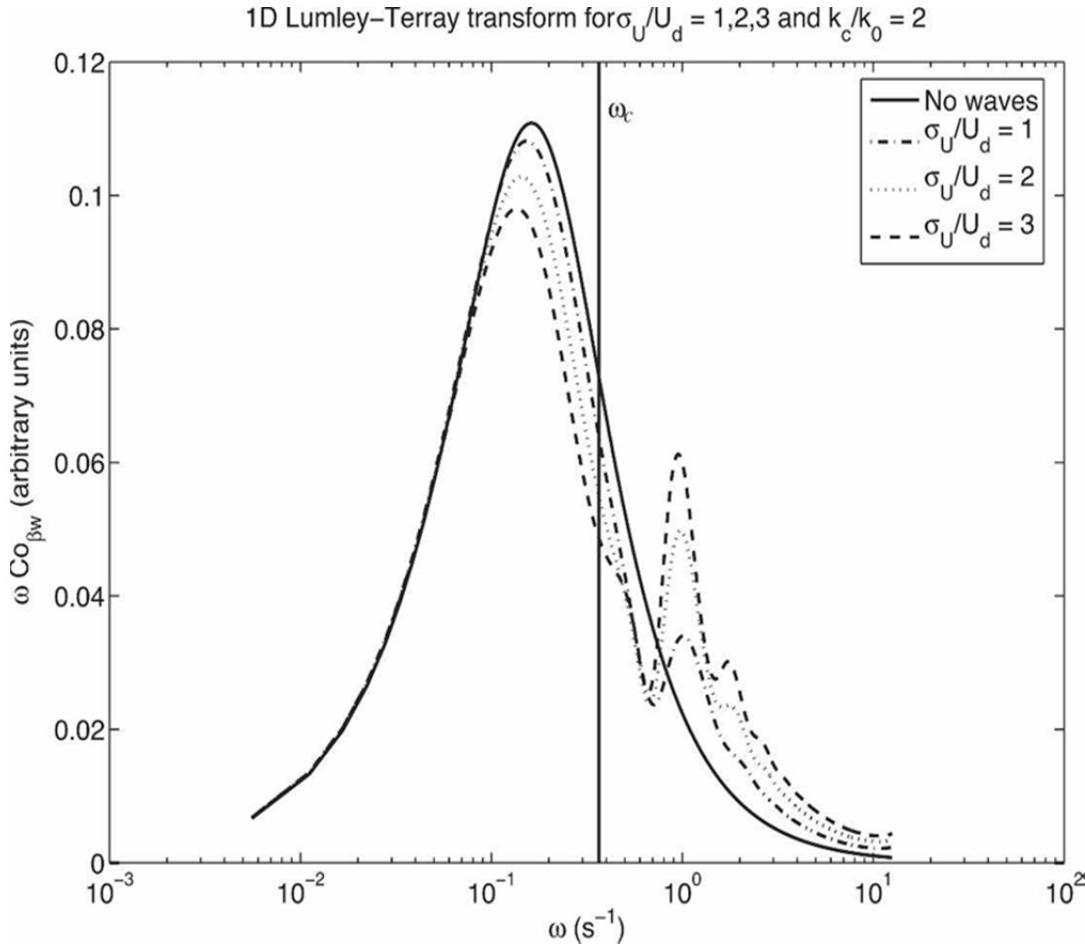
"This represents the frequency domain variance-preserving cospectra of unsteadily advected frozen turbulence whose wavenumber spectrum is described by the semitheoretical prediction of the turbulence cospectra as a function of wavenumber. The wave band cutoff, ω_c, is shown by the vertical line at 0.38 s^{-1}. As the wave energy increases, the effects of the unsteady advection shift more energy from below-wave-band frequencies to wave band frequencies and decrease the apparent rolloff frequency. To examine larger wave effects σ_U/U_d was used, where σ_U is the standard deviation of wave velocities and U_d is the steady drift speed." Source: Gerbi, G. P., J. H. Trowbridge, J. B. Edson, A. J. Plueddemann, E. A. Terray, and J. J. Fredericks, 2008: Measurements of momentum and heat transfer across the air–sea interface. *J. Phys. Oceanogr.*, **38**, 1054–1072.Source: Gerbi et al. 2008.

3.   **Predicting Turbulence Cospectra in the Frequency Domain and as a Function of Wavenumber**

To form the cospectra between turbulent fluctuating horizontal and vertical velocity components of the flow each components that make up the instantaneous

velocities in the x, y, and z directions as denoted by u, v, and w are required is broken down as

$$u = \tilde{u} + \bar{u} + u', \tag{1.14}$$

where $\tilde{u}$ represents the wave induced perturbations, $\bar{u}$ is the time mean over the length of the ensemble, and u' describes the turbulent perturbations. The turbulent velocities u' and w' are related to the vertical Reynold's Stress (τ) via

$$\tau = \rho_o(-\overline{u'w'}), \tag{1.15}$$

where ρ_o is the reference density and $\overline{u'w'}$ is the covariance. Following Gerbi et al. 2008, to estimate Reynolds stresses under waves from Eulerian velocity observations, a shape function for the modification of the cospectrum is developed:

$$\frac{Co_{uw}(k)}{\overline{u'w'}} = A\frac{1/k_o}{1+\left(\dfrac{k}{k_o}\right)^{7/3}}, \tag{1.16}$$

where k is the wave number, k_o is the rolloff wave number representing the inverse of the turbulent eddy length scale,

$$k_o = 1/L, \tag{1.17}$$

and

$$A = \frac{7}{3\pi}\sin\left(\frac{3\pi}{7}\right). \tag{1.18}$$

The rolloff wavenumber identifies the location of the peak for the variance preserving spectrum. In this form the cospectra is relatively constant for small wave numbers and rolls off at a $k^{-7/3}$ rate for high wave numbers. In the frequency domain the cospectrum $Ko_{uw}(\omega)$ is derived in part using Equation 1.16

$$Ko_{uw}(\omega) = \frac{1}{2\pi}\int\limits_{-\infty}^{+\infty}dT\int\limits_{-\infty}^{+\infty}dk\frac{Co_{uw}(k)}{2}\times e^{iT(kU_d-\omega)}e^{k^2[c(T)-c(0)]}, \tag{1.19}$$

where $c(T)$ is the temporal autocorrelation function of the wave displacement defined by

$$c(T) = \frac{1}{2\pi}\int\limits_{-\omega_{max}}^{+\omega_{max}}d\omega\frac{S_{uu}(\omega)+S_{vv}(\omega)}{\omega^2}, \tag{1.20}$$

where $S_{uu}(\omega)$ and $S_{vv}(\omega)$ are the two-sided autospectra for the horizontal velocities and the radian frequency (ω) is related to the frequency (f) by the expression

11

$$f = \frac{\omega}{2\pi}. \qquad (1.21)$$

Equation 1.20 estimates wave displacements using relation between the autospectra and normalizing by the radian frequency result in a rapid decay due to the frequency squared term (Gerbi et al. 2008).

Using Equations 1.16 through 1.21, semitheoretical spectra were generated as shown in Figure 3. In this figure, the effects of increased wave energy is parameterized by

$$\sigma_U / U_d, \qquad (1.22)$$

where σ_U is the standard deviation of wave velocities and U_d is the steady drift speed. The widening of the spectral peak along with a spectral peak decrease with increasing wave orbital velocity can be seen in Figure 3, confirms that unsteady advected frozen turbulence has relatively more energy in the wave band and less energy below the wave band. Additionally, it is important to note the proximity of the cutoff wave number (k_c) to the rolloff wavenumber (k_0),

$$k_c / k_0, \qquad (1.23)$$

noting that the cutoff wave number is a property of the wave field and the rolloff wavenumber is a property of the turbulence. The relation between Equation 1.22 and 1.23 defines the magnitude of the spectral peak's distortion. A small value for the ratio of cutoff wave number over the rolloff wavenumber and large values for the ratio of the standard deviation of wave velocities and steady drift speed will result in significant errors when estimating the covariance and rolloff wavenumber (Gerbi et al. 2008).

Using the simulated spectra shown in Figure 3, Gerbi et al. (2008) found that the ratio of the standard deviation of wave velocities and steady drift speed yielded values less than or equal to 2; therefore, the steadily advected form (Equation 1.12) of the frozen turbulence could be used to perform the transformation from observed frequencies to wavenumber values.

Applying the frozen turbulence hypothesis and estimating the turbulence cospectra are important concepts when analyzing turbulence however, they can readily be contaminated by the large wave orbital velocities. It is therefore necessary review an additional method to the TDM that may prove to be a more effective method in our case where our observations are limited by lower wind speeds.

4.   Separating Waves and Turbulence

Two differences between waves and turbulence are the differences in spatial and temporal scales associated with each, and that wave velocities near the surface are characteristically much larger than turbulent. The strong wave orbital motions results in the aliasing of some low wavenumber energy into the wave band as a result of unsteady advection for an Eulerian sensor (Gerbi et al. 2008).

To perform the separation a wave band cutoff frequency (ω_c), as seen in Figure 3, must be calculated as the area below this cutoff line is considered to be dominated by turbulent motions. To calculate the wave band cutoff the orbital vertical velocity spectrum is estimated from the pressure spectrum (S_{pp})

$$S_{ww}^{(p)} = S_{pp} \frac{k^2}{\rho_0^2 \omega^2} \tanh^2 k(z+h),$$
(1.24)

where h is the water depth. Outside of the surface gravity wave frequency band, vertical velocity spectrum derived from velocity measurements (S_{ww}) are expected to be greater than those of vertical velocity spectrum derived from pressure measurements ($S_{ww}^{(p)}$). Gerbi 2008 chose the wave-band-cutoff frequency to be when the condition

$$S_{ww}^{(p)}(\omega_c) = 0.3 S_{ww}(\omega_c),$$
(1.25)

was met. Additionally, the cutoff frequency and Equation 1.12 can be used to compute the cutoff wavenumber (k_c), identifying the minimum resolvable length scale for the below-wave band turbulence. Typically the minimum resolvable length scales are less than twice the measurement depth (Gerbi et al. 2008).

Unsteady advection, a wide range of scales, complex motion paths as a result of wave-turbulence interactions all make it difficult enough to separate out the turbulent

motions. The additional effects of Langmuir circulations add further complications to the process. Wilczak and Tillman (1980) found turbulent eddies had longer length scales in the wind stress parallel direction and elongated convective plumes were present in the downwind direction possibly indicating the influence of Langmuir circulations. Therefore, Langmuir circulation is another important factor to consider when in the study of turbulent stresses under wind-forced waves.

5.   The Role of Langmuir Circulation

Langmuir Cells were first discussed by Langmuir (1938), and were observed to be counter-rotating vortices that were aligned with the wind flow. The areas between adjacent cells formed a convergent region often defined by the presence of flotsam; the associated flow between these cells became known as Langmuir circulation. Prior to a filed study by Weller and Price (1988) the role of Langmuir circulation in the mixing and vertical redistribution within the mixed layer, and upper ocean dynamics had not been clear. Weller and Price (1988) indicated that Langmuir circulations were typically characterized by downward vertical velocities less than or equal to 5 cm s^{-1}. Additionally, there were no profile measurements conducted to capture the entire upper layer's characteristics, thus leading to the uncertainty of their role in vertical transfers. Momentum transfer from wind to the ocean had been assumed to be accomplished through a classic turbulent surface boundary layer extending down from the ocean surface.

Weller and Price 1988 found compelling evidence through their observations conducted across three cruises onboard the Research Platform *Flip* that Langmuir circulation contributed to entrainment processes in the ocean mixed layer. Their three cruises took place during December 1982, May 1983, and October through November 1983. To capture velocity profiles spanning the ocean mixed layer into the pycnocline between surface and 165 m they used a combination of fixed depth Vector Measuring Current Meters (VMCM) and a profiling Real Time Profilers (RTP) (Figure 4). Computer punch cards were used for surface visualization of convergence zones as seen in Figure 5. The velocity data collected on the December 1982 cruise allow development of a conceptual model of Langmuir circulation shown by Figure 6b.   Strong downward

14

motions and weaker upward motion associated with the Langmuir circulation are seen in the profile time series data in Figure 6a. Based on the RTP data, it was noted that the presence of greater velocities than previously recorded existed, up to 27 cm s^{-1}, however typical vertical velocities were generally observed between .025 to .1 m s^{-1}. The velocity maxima were found to be below the surface and above mixed layer median depth. The areas of strongest vertical shear were also found to occur at the areas of convergence and decrease in the area between cells.

The velocity profiles indicated the presence of a downwind jet along the area of convergence. Looking at the mean downwind flow across multiple cells, they deduced that the vertical transport of horizontal momentum by Langmuir cells was mixed layer depth dependent. This meant that the downwind flow in the near surface layer was greater at the deeper depths (6.5 m) than at shallower depths (2 m) (Figure 6).

Figure 4.   The Real Time Profiler
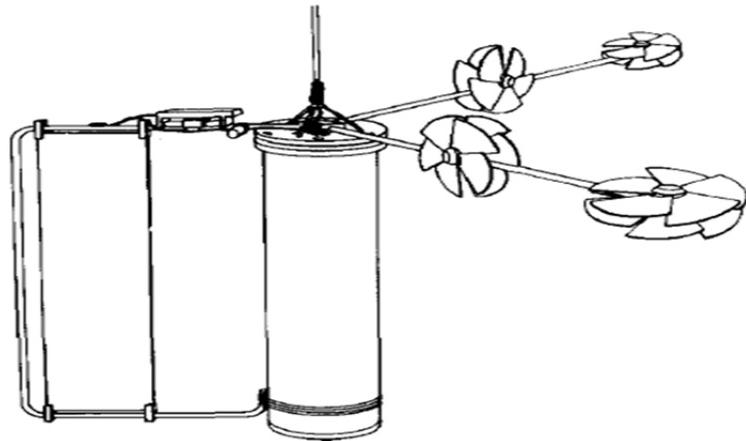
"Two dual-propeller VMCM sensors mounted at right angles provided measurements of the three orthogonal components of velocity (with two redundant measurements of the vertical component). A Seabird conductivity cell and a temperature sensor are mounted on the top of a frame that supports a fin for orienting the instrument relative to the flow." Source: Weller, R. A., and J. F Price, 1988: Langmuir circulation within the oceanic mixed layer. *Deep-Sea Res.* **35**: 711–747.

Figure 5.   IBM Computer Cards on the Surface
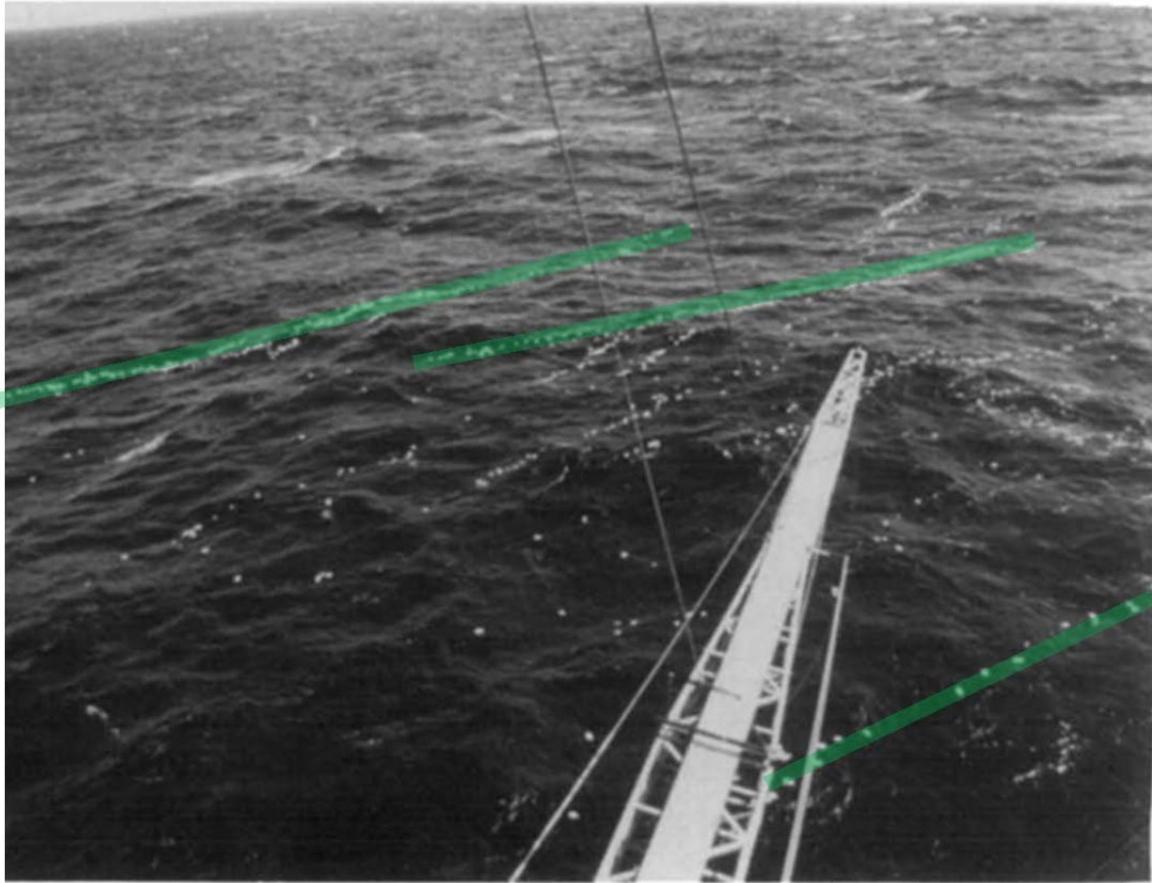
Photograph of computer cards (   ) on the sea surface showing the convergence zones between Langmuir Cells. The instruments are suspended beneath the booms as the ship drifts through the regions of convergent flow marked by these lines of computer cards. Source: Weller, R. A., and J. F Price, 1988: Langmuir circulation within the oceanic mixed layer. *Deep-Sea Res.* **35**: 711–747.

Figure 6.   Langmuir Circulations and December 1982 RTP Data
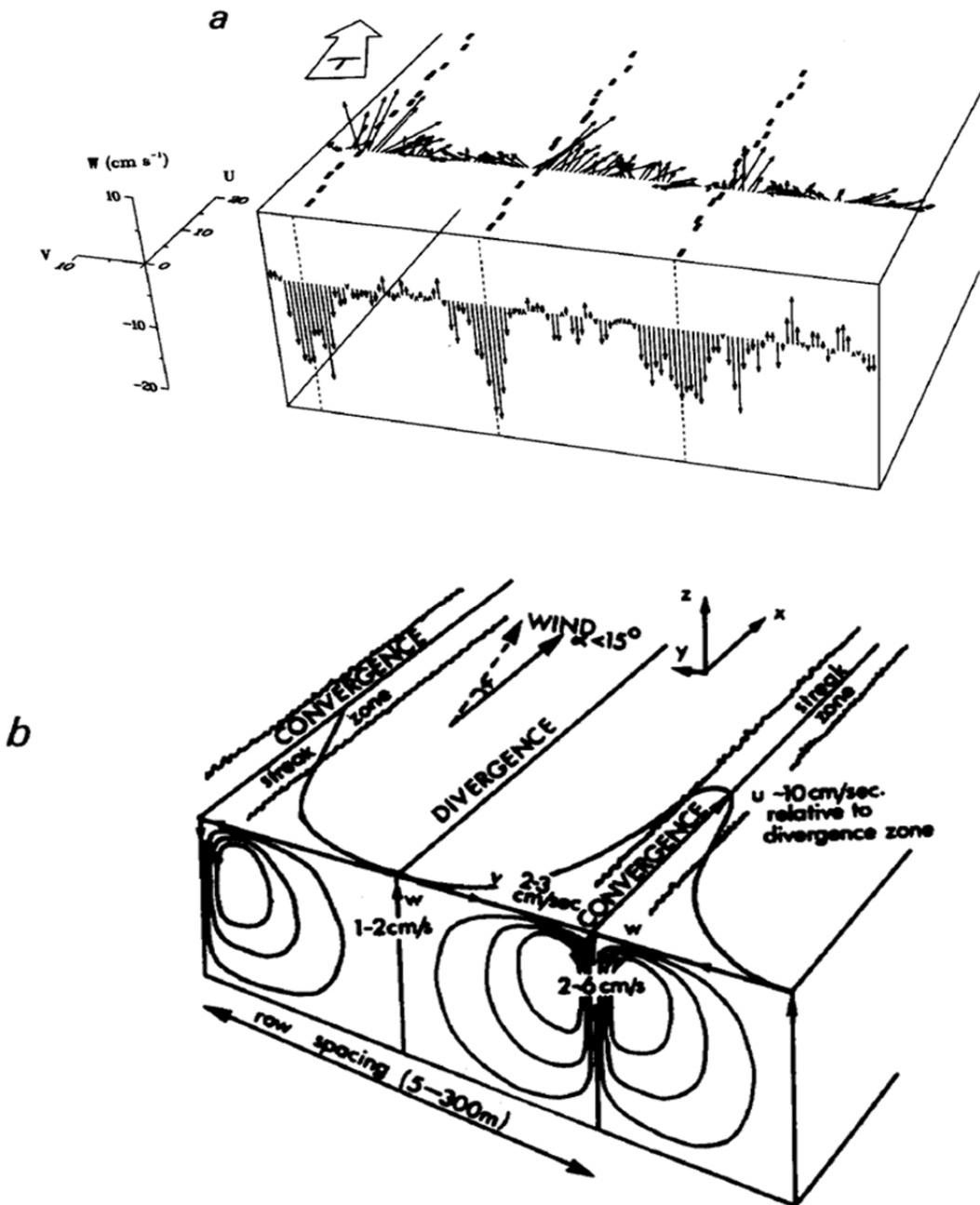
"Comparison of RTP data (a) from the December 1982 cruise (as shown in Weller et al. 1985) with Pollard's (1977) visualization (b) of Langmuir circulation. In (a) 30 min of data from the RTP are shown that were collected with the instrument parked at a depth of 23 m. Vertical velocity data subjected to a 3-point running mean are shown on the forward face of the figure, and horizontal velocity data from the same depth (23 m) are shown on the top surface. The downwelling and downwind velocity signals were encountered by the RTP in convergence regions marked by computer cards" shown in (a). Source: Weller, R. A., and J. F Price, 1988: Langmuir circulation within the oceanic mixed layer. *Deep-Sea Res.* **35**: 711–747.

Of the three cruises conducted on *Flip* by Weller and Price (1988), the data collection efforts conducted during the Mixed Layer Dynamics Experiment (MILDEX) through October and November 1983 were the most comprehensive. High levels of wind forcing variability revealed the presence of multiple vertical velocity scales associated with Langmuir circulations existed. During developing wind events, a multiplicity of scales was observed, and once the circulation stabilized, they became characterized by larger scales. The use of the computer cards on the surface identified this cycle by their transition from small to large spacing between lines over time with maximum spacing between cells three times the depth of the mixed layer. Though the Langmuir cells were found to be transient, gaps between measurements in the vertical profile did not allow the data from either study to resolve the cells well enough to fully capture their growth, decay and motion. In addition to scaling variability, the MILDEX data set showed that that Langmuir cells contributed to the energy content and the near surface shear in the frequency band between 2 and 10 cycles per hour (cph), as shown by the peak in the vertical shear energy spectrum in Figure 7. The ensemble low frequency energy peak was found to be a result of the long vortical flows spanning half of the mixed layer advecting past the Eulerian sensors. Additionally, a higher maximum vertical shear was found to coincide with periods of rapid increase in wind, as shown by the red boxed region in Figure 8.

Figure 7.   Rotary Autospectra of the Vertical Shear November 9, 1983
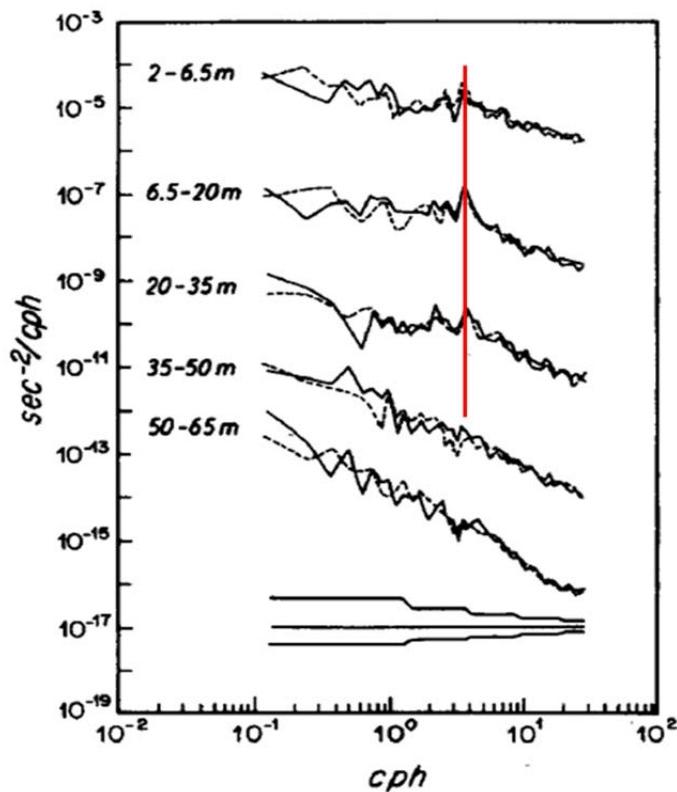
"Rotary autospectra of the vertical shear of horizontal velocity for November 9, 1983 from five depth pairs, 2–6.5 m, 6.5–20 m, 20–35 m, 35–50 m, and 50–65 m. The top spectrum is at the proper location relative to the vertical axis; each spectrum below is shifted down an additional two decades. The solid line is the clockwise spectrum; the dashed line is the counter-clockwise spectrum. The 95% confidence limits are indicated." The red line indicates the peaks within the mixed layer down to 35 m, beyond which shear is dominated by low frequency variability. Source: Weller, R. A., and J. F Price, 1988: Langmuir circulation within the oceanic mixed layer. *Deep-Sea Res.* **35**: 711–747.

19

Figure 8.   MILDEX Observation Data
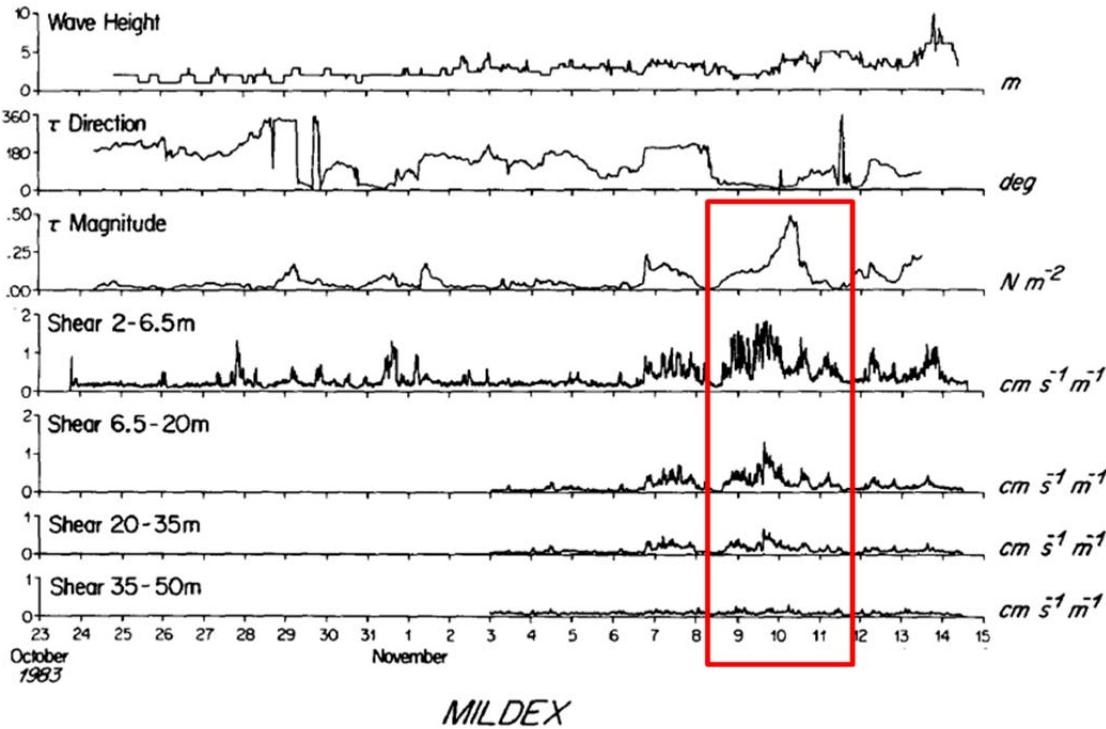
"Time series of wave height (eyeball observation), direction of the wind stress (direction toward), magnitude of the wind stress, and magnitude of the shear in the 2–14 cph band at depth pairs 2–6.5 m, 6.5–20 m, 20–35 m, and 25–50 m." The red box shows the correlation between the increase in wind magnitude with a peak in the vertical shear that transfers down to around 35m depth. Source: Weller, R. A., and J. F Price, 1988: Langmuir circulation within the oceanic mixed layer. *Deep-Sea Res*. **35**: 711–747.

This study allowed the role of Langmuir circulation in breaking up stratification below the mixed layer versus the role boundary layer turbulence (BLT) to be investigated. Their conclusion was that Langmuir circulations maintained mixing in the upper mixed layer, while BLT was the mechanism that dominated entrainment at the base of the mixed layer since Langmuir circulations had little effect on mixing the bottom half to two thirds of the mixed layer (Weller and Price 1988).

In the shallow water coastal region, Marimorino et al. (2005) noted banded structures that resulted from bottom sediments suspended in upwelling regions of Langmuir circulations in the Gulf of Mexico. The spacing between streaks was found to be 10 times the vertical Langmuir cell extent, which is much greater than what Weller

20

and Price found. The greater horizontal scale in shallow water resulted in LSC's major impact on sediment and bioactive material transport in the shallow coastal regions.

More recently, Gargett and Wells (2007) utilized a five-beam acoustic Doppler current profiler (VADCP) to study Langmuir circulation in coastal waters. The VADCP is a commercial Doppler current profiler with a four-beam Janus configuration transducer set with an additional center beam to better resolve vertical velocity profiles. It is important to note that the VADCP's monostatic configuration caused the effective sample volume to resolve three components of velocity to equal the range, or half the range for solutions using the central beam, resulting in requiring uniform velocity fields across the 15 m beam aperture near the surface. The system setups for these observations were 0.4 m vertical bins with a sample interval of ~1 second.

Gargett and Wells (2007) deployed the VADCP on a shallow continental shelf location where the Langmuir cells would cover the full extent of the water column. Cells of this type became known as Langmuir supercells (LSC). Their study identified the presence of Langmuir circulation using qualities identified by previous studies:

1. "Downwind jets are situated under downwelling regions" (Gargett and Wells 2007, p. 57).

2. "Downwelling regions are narrower than upwelling regions" (Gargett and Wells 2007, p. 57).

3. "Vertical asymmetry of the crosswind flow is also referred to as surface intensification" (Gargett and Wells 2007, p. 57).

4. "Correct phasing of crosswind is relative to vertical velocities, given the direction of crosswind advection past a fixed instrument" (Gargett and Wells 2007, p. 57).

5. "Maximum vertical velocity is in the upper half of the water column "(Gargett and Wells 2007, p. 57).

In Figure 9 the velocity profile time series from the VADCP show the strong downwind jet in panel (c) and the strong downward velocity in panel (b) during the LSC event marked by the black line. The concurrence of these velocity components identifies this area to be the converging downwelling region between Langmuir cells. Panel (e) is a schematic of the circulations associated with the LSC event showing a strong downwind

21

jet denoted by the circle with the x in the downwelling region. Additionally, a zoomed in section of Figure 9 shows two very different scale features. A large feature, found to be an LSC event denoted by L and a shorter period event described by area S. Event L was found to be modulated by the shorter period variability event like the one described by S (Figure 10). This provides evidence of two distinct scales of variability acting with the Langmuir cells (Gargett and Wells 2007)

Figure 9.   Depth versus Time Fluctuations
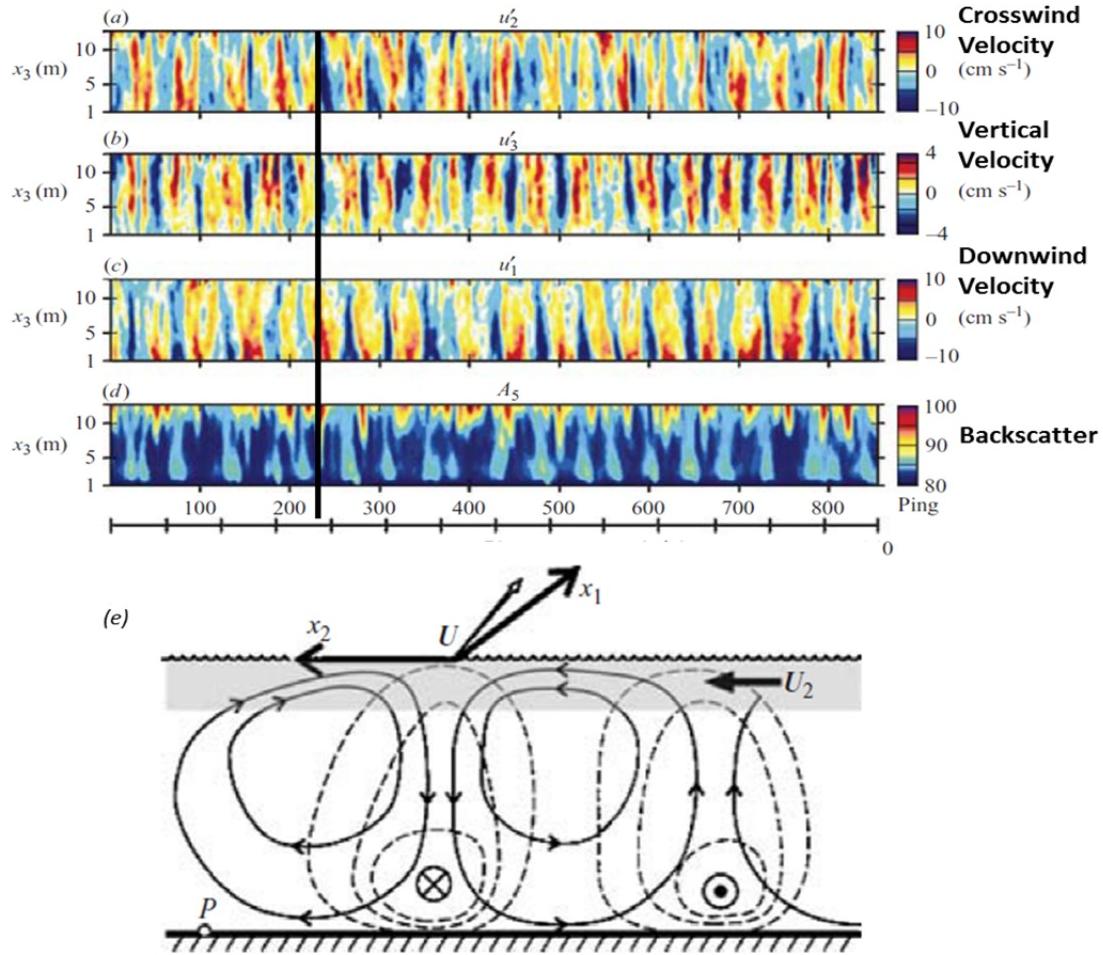
"An example of depth/time fluctuations of the (a) crosswind velocity u_2', (b) vertical velocity u_3' (c) downwind velocity u_1', and (d) vertical beam backscatter amplitude A5 for a record (43.025) within the LSC episode. The sampling period is 9.6 s: the total record length is~2.3 h. As described in § 4.2.2, the fluctuating velocity field is that left after a linear least-squares fit at each bin has removed a slowly varying "mean" velocity associated with a combined wind and tidally forced flow. The vertical line draws attention to synchronous features mentioned in the text. (e) Features of the cellular velocity structure observed during episodes of LSC: drawn for record 43.025 which has crosswind mean flow U2 >0." Positive values represent the crosswind component in the x_2 direction seen in panel (e), upward vertical velocity, and in the downwind direction for downwind velocities. Source: Gargett, A., and J. R.Wells, 2007: Langmuir turbulence in shallow water. Part 1. Observations. *J. Fluid Mech.* **576**, 27–61.

Figure 10.   Examples of LSC Spatial and Time Scale of Variability
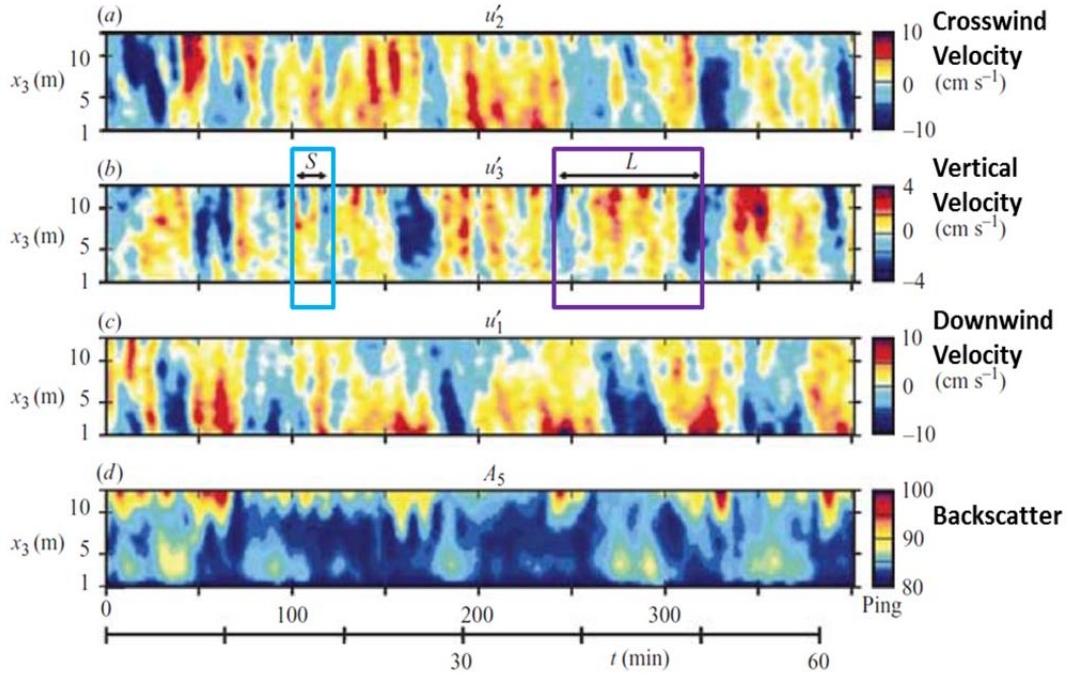
"Using the same axis as Figure 9, this illustrates an enlarged portion of record 43.024 showing the existence of two distinctly different space/time scales of variability, clearly visible in both velocity and backscatter fields, during periods of LSC. The longer period (~8–17 min) features (L), identified here as LSC, are modulated by shorter period (~1–1.5min) variability (S)." Source: Gargett, A., and J. R.Wells, 2007: Langmuir turbulence in shallow water. Part 1. Observations. *J. Fluid Mech.* **576**, 27–61.

24

II. BACKGROUND

A. COUPLED BOUNDARY LAYERS AND AIR-SEA TRANSFER PROGRAM

In an effort to investigate coupled ocean-atmosphere processes the Coupled Boundary Layers and Air-Sea Transfer (CBLAST) Department Research Initiative (DRI) was created by the Office of Naval Research (ONR). The main goal of the CBLAST program was to improve parameterizations of momentum fluxes across the air-sea interface in an effort to develop fully coupled two way models that capture the surface boundary conditions, thus improving shorter time scaled weather forecasts (Figure 11). Coupling across the air-sea interface plays a vital role in larger scale storms such as hurricanes, which depend greatly on heat, mass, and momentum exchanges between the ocean and atmosphere to determine their intensity. To ensure both extremes were well observed they developed CBLAST-LOW and CBLAST-Hurricane projects (Edson et al. 2007).

This thesis's research is directed at the CBLAST-LOW objectives which focuses on the coupled boundary layer (CBL) processes associated with the low wind conditions. The observations ranged from those with insignificant wind stress dominated by buoyant forcing to those where wave breaking and Langmuir circulation were important factors in the exchange process (Edson et al. 2007). The research conducted in the current thesis experiment concentrated on the range influenced by wave breaking and Langmuir circulation in an effort to capture turbulent stresses, shear, and kinetic energy dissipation rates below wind driven surface gravity waves.

Figure 11.   Key Air -Sea Interactions
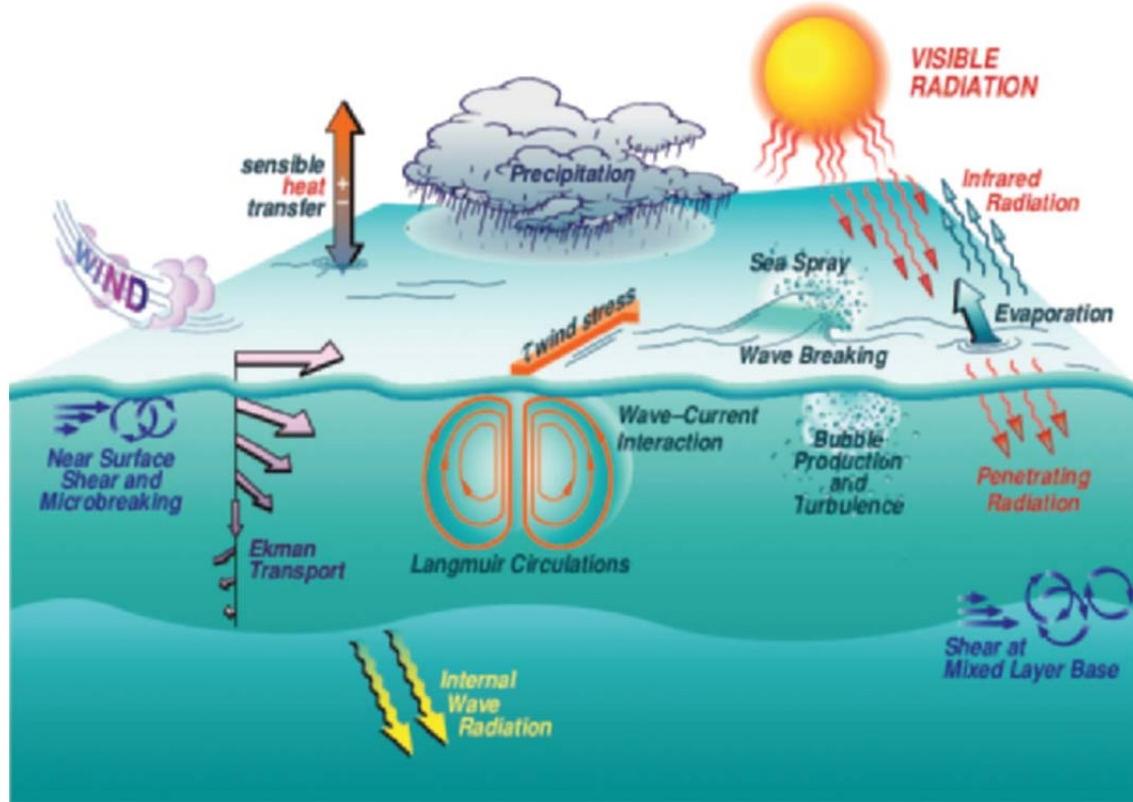
"Key physical processes governing air-sea exchange across the coupled boundary layer."
Source: Edson J., T. Crawford, J. Crescenti, T. Farrar, J. French, et al. 2007: The coupled boundary layers and air-sea transfer experiment in low winds (CBLAST-Low). *Bull. Am. Meteorol. Soc.* **88**,342–56.

In line with the CBLAST-LOW's main goal to improve parametrization for the Naval Research Laboratory's (NRL) Coupled Ocean-Atmosphere Mesoscale Prediction System (COAMPS) and the Regional Ocean Modeling System (ROMS) at low wind conditions, the summer months in this region with winds typically southwesterly at 2–6 meters per second (Edson et al. 2007) were selected. Sub-grid scale processes including momentum transfer in the presence of waves remain problems in models such as ROMS and COAMPS. For example, the influence of Langmuir circulations and intermittent turbulence resulting from wave breaking is important and rarely accounted for in most flux-profile relations utilized in models (Edson et al. 2007).

During CBLAST an upward looking Bistatic Coherent Doppler Velocity Profiler (BCDVP) developed in the Ocean Turbulence group at Naval Postgraduate School (NPS)

(Stanton 2001) was used for the first time near Martha's Vineyard providing 1-cm vertical resolution profiles of the three component velocity field upwards into the wave crest–trough region. The BCDVP's purpose was to capture the effects of intermittent wave breaking, Langmuir circulation, and turbulence generated by shear and convective instabilities associated with wind generated waves. For this reason the BCDVP will serve as one of the keystone instruments used at the Salinas River and Elkhorn Slough in California for this thesis research on momentum transfer caused by wind generated waves at the air-sea interface.

Using the foundations set forth by the initial efforts of CBLAST, this thesis will again utilize the BCDVP to attempt to observe the influence of Langmuir circulations and effects of wind stress on the momentum transfer across the air-sea interface (Figure 11). The production of wind generated surface gravity waves should generate resolvable turbulence granted the winds reach a sufficient sustained velocity across the maximum fetch possible at either of the designated research locations.

B.   AREAS OF STUDY

Initially there were two areas that we deployed our sensors in an effort to collect the necessary data to conduct our analysis of the Ocean surface boundary layer (OSBL) and atmospheric boundary layer (ABL). California's Elkhorn Slough and Salinas River were the selected sites for our research. Both sites were in the local area, provided adequate depth, had the potential to provide adequate wave fetch distances, and strong enough wind speeds to facilitate wave breaking. Their orientation took advantage of the commonly occurring west-northwesterly summer sea breeze.

1.   Elkhorn Slough, California

Elkhorn Slough, California, is located north of Monterey, California at approximately 36.825°N, 121.757°W. Accessed via the Moonglow Dairy, this is a tidally influenced saltwater estuary that connects with the Moss Landing Harbor. It has a predominant east-west orientation with a bend that provided an extended northwest-southeast fetch that aligns with the characteristically observed west-northwesterly sea breeze associated with this area. Though this site proved to be affected by minimal swell

(Figure 13), it did not to provide the adequate fetch for the observed wind speeds to produce breaking waves (Figure 12) and had strong tidal elevation changes and tidal currents. The data collected during the March 24, 2015, deployment yielded had wind forcing significantly less than was needed to study wind/wave conditions approaching wave breaking. The tidal elevation range coupled with the limited BCDV profiling range reduced the usefulness of this site, so a site on a blocked branch of the Salinas River was investigated.

Figure 12.   Fetch and Predominate Winds during Data Collection
Effort on March 24, 2015

Portrayal of the fetch associated with the average wind direction and speed during the time the sensor was deployed. Note the clusters of buildings just off the slough; these belong to the Moonglow Dairy. The insets show conditions during the sensor deployment and a visual representation of the fetch distance during a site survey. The slough's predominantly east-west orientation provides a limited fetch for the waves to build (maximum possible fetch around 850m from the bend in the slough) before reaching the deployment site ( ). Map created in Google Earth, October 12, 2015, http://www.google.com/earth/.

Figure 13.   Elevations around the Deployment Area at Elkhorn Slough, California
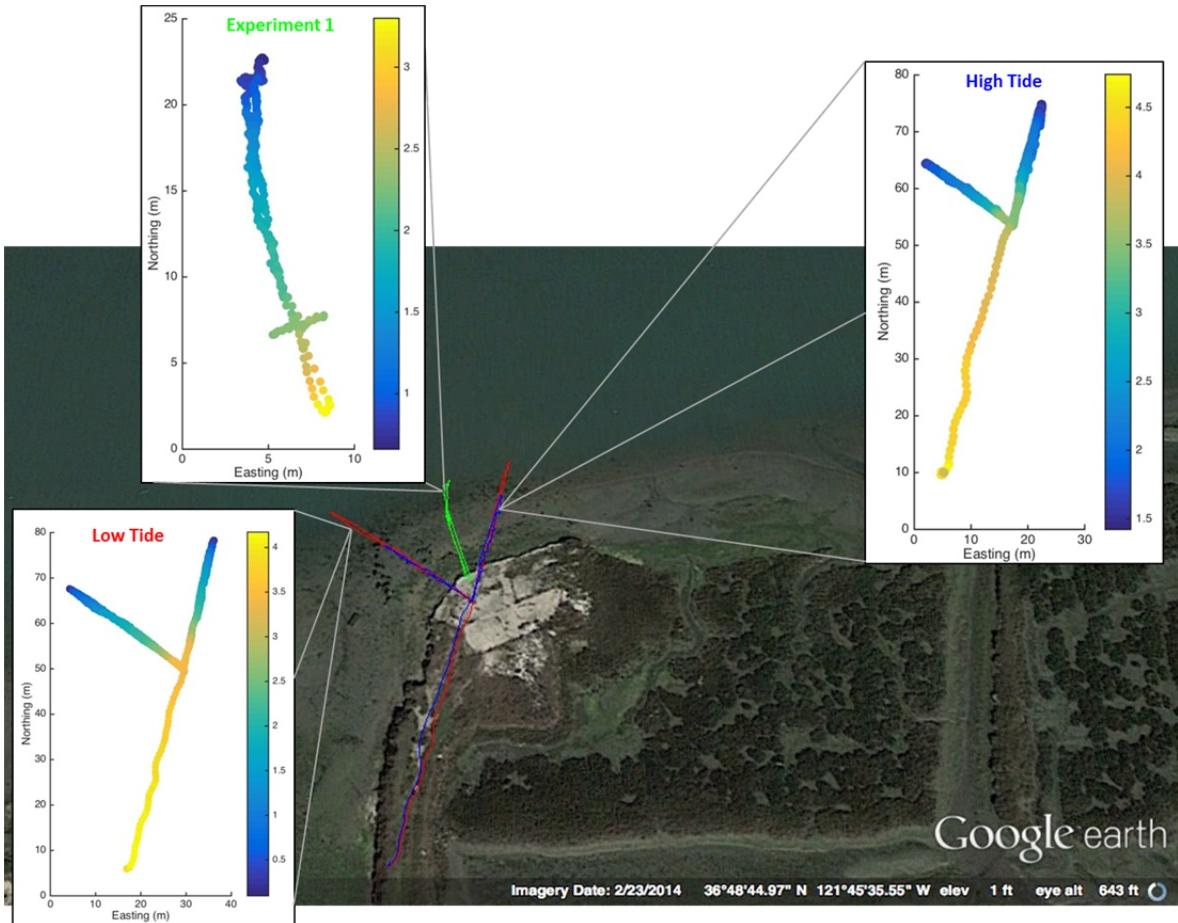
Elkhorn Slough, California, with transects overlain onto Google earth to illustrate the variations in elevation between high and low tides compared to when the data was collected. Map created in Google Earth, October 12, 2015, http://www.google.com/earth/.

2.   Salinas River, California

The area of the Salinas River chosen to deploy our sensors was located on the Salinas River National Wildlife Refuge located at approximately 36.738°N, 121.794°W (Figure 14). For access to the river a permit from the U.S. Fish and Wildlife Services was required to conduct research. The river's northwest-southeast orientation provided an ideal fetch for capturing the commonly observed summer northwesterly sea breeze. A survey of the deployment area using a high resolution acoustic depth sounder yielded ideal depths for deploying the BCDVP with a maximum depth around 2.2 meters (Figure 15). Figure 14 shows a time when the river is closed off from the ocean. Tidal and swell

influences on the river are nonexistent in the summer conditions chosen for these observations.

The initial site visit to the Salinas River included the quick look at the bathymetry using an altimeter in conjunction with a Global Positioning System (GPS) receiver and a visual look at any other influential factors such as the algae growth state. Depth survey results from a digital altimeter/GPS instrumented kayak (Figure 15) identified a suitable BCDVP deployment location of 36°44.290′ N, 121°47.638 W (Figure 16) characterized by an average depth of approximately 1.6 meters. A visual review of the orientation with regard to the dominant wind direction, river width, bank steepness, and algae growth state further supported it as a favorable data collection site.

This survey showed that the Salinas River was a favorable site, however it is important to note the presence of surface algae growth that typically covers the surface during the late summer months. The presence of surface algae is critical as it dampens out surface wind waves reducing the ability to have well characterized fetch-limited waves. For the May sensor deployment it did not create any issues however, however by August most of the river's surface was covered by algae. Since the river does not flow in the summer months due to lack of inflow to raise its levels high enough to overflow into the ocean, the algae patches tend to float in response to wind forcing until the fall and winter months when sufficient rain and lower temperatures reduce the algae levels (Figure 15). Despite its susceptibility to algal influence, the Salinas River proved to be a favorable location to conduct a study of the below wave turbulent structures associated with wind generated surface gravity waves.

Figure 14.   Salinas River Overview
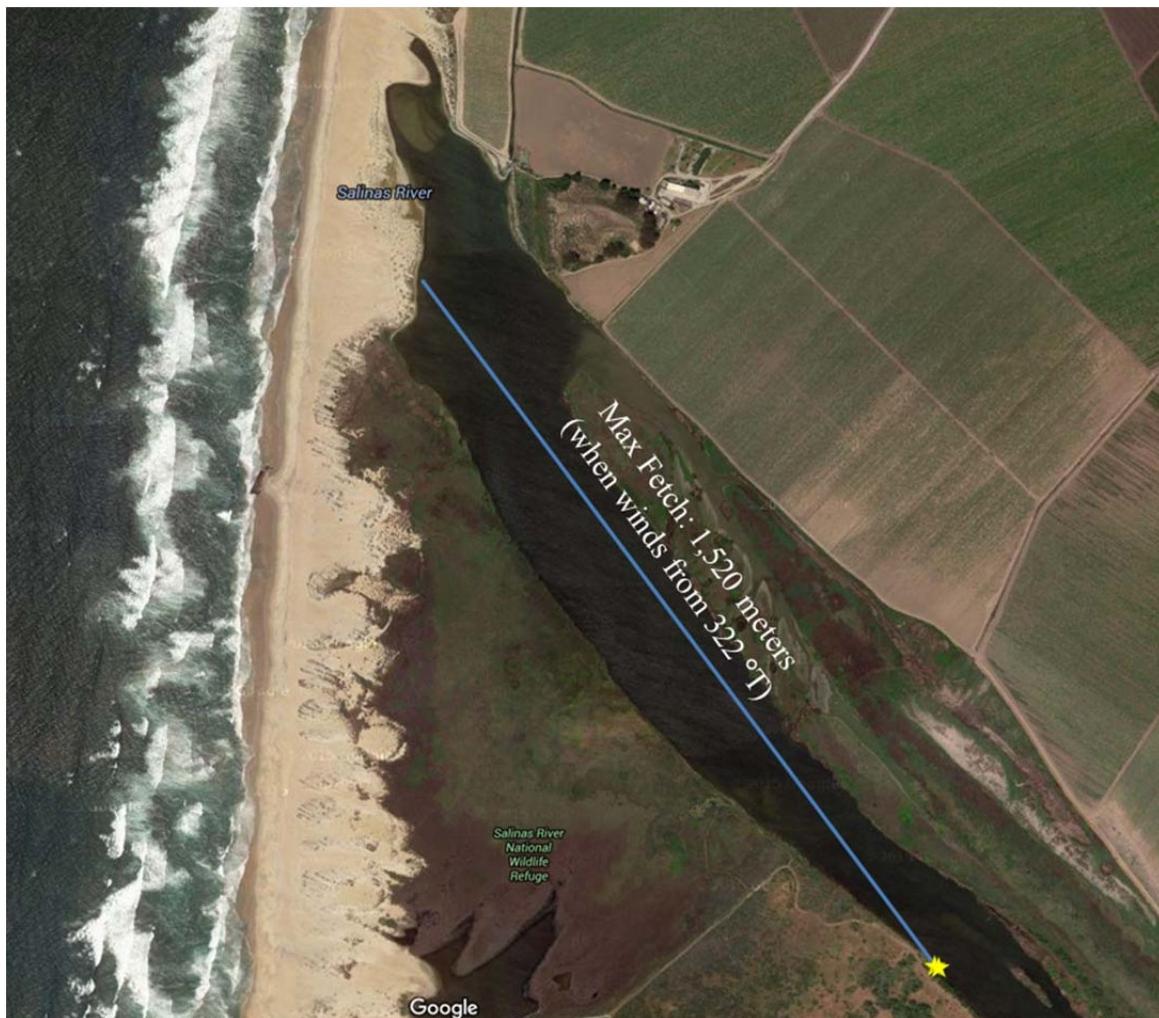
Google earth image of the portion of the Salinas River that is part of the Salinas River National Wildlife Refuge. The river's predominantly northwest-southeast orientation provides an extended fetch for wind waves to build (Maximum possible fetch around 1,520 m from the mouth of the river to the deployment site ⭐). Map created in Google Earth, October 12, 2015, http://www.google.com/earth/.

Figure 15.   Bathymetry of Deployment Area Salinas River, California
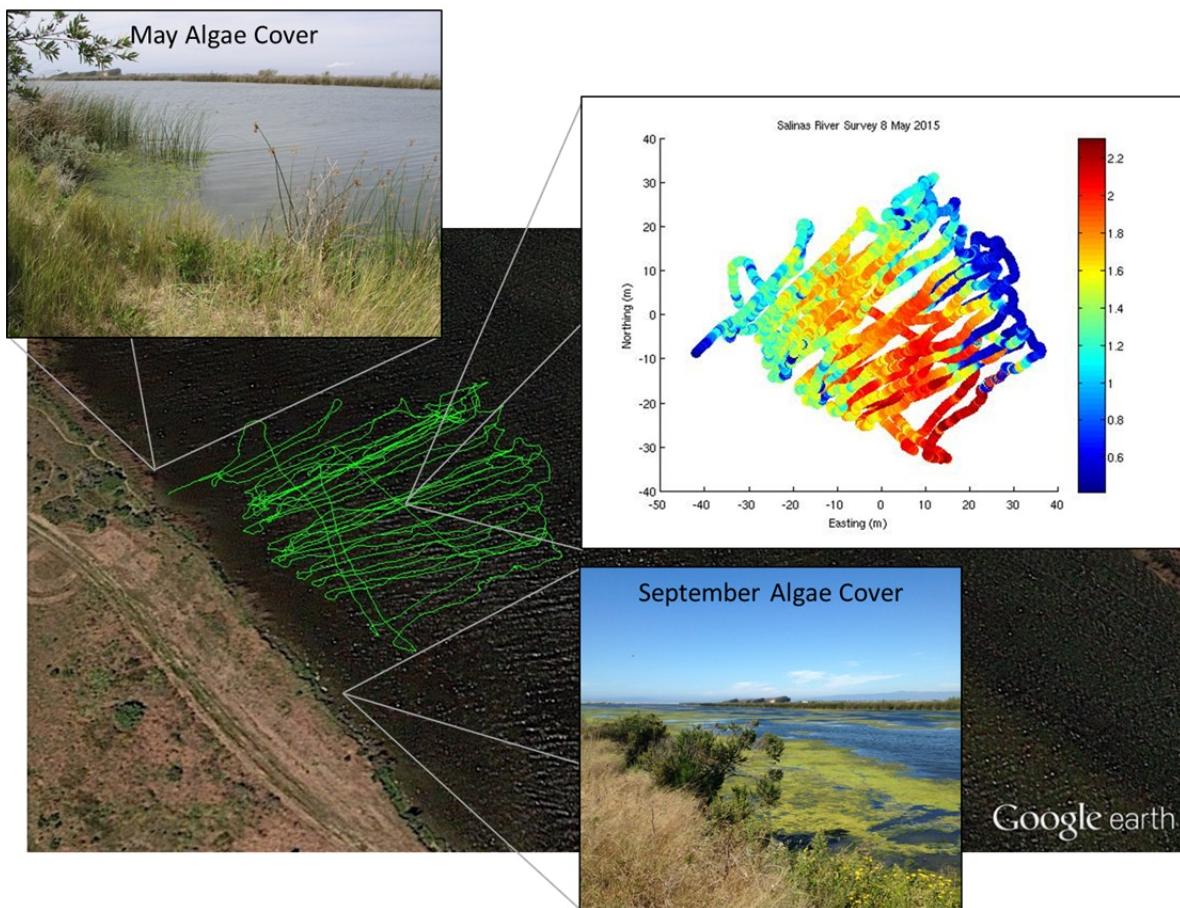
Salinas River, California, with transects overlain onto Google earth to illustrate the various depths in meters at the proposed deployment site. The *x*-axis and *y*-axis are in meters to aid with scaling for the visualization of transects. Note the significant difference in surface algal growth between May and September 2015. Map created in Google Earth, October 12, 2015, http://www.google.com/earth/.

Figure 16.   Salinas River Survey Data Collection Setup
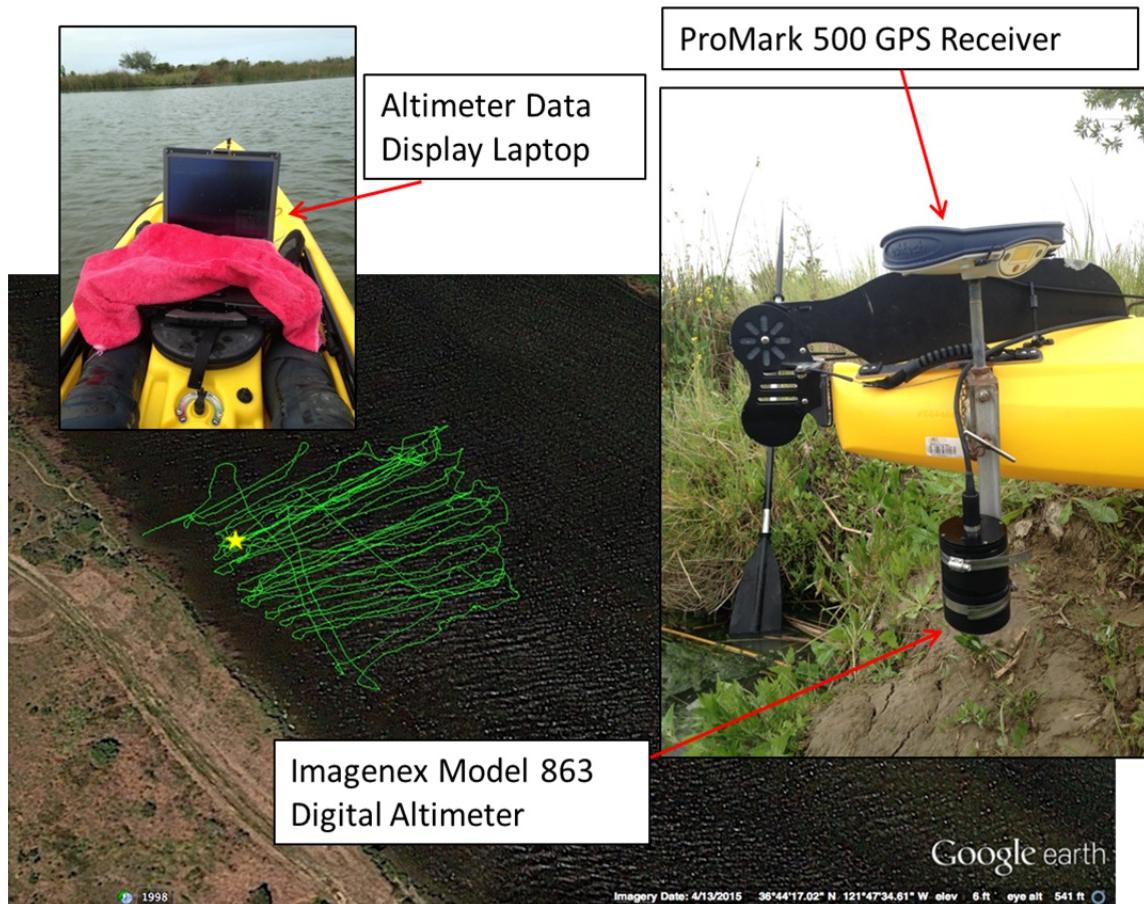
The sensor setup on the survey kayak used to collect the data displayed in Figure 15. The sensor depth was accounted for during depth calculations and was 0.1778 meters below the surface. Based on the BCDVP's setup, a deployment site was chosen with an ideal depth around 1.6 meters (⭐). Map created in Google Earth, October 12, 2015, http://www.google.com/earth/.

III. INSTRUMENTATION

Key sensors used for data collection were assembled and tested both in the Ocean Turbulence Lab at NPS and in the field prior to its deployment at the Salinas River. Sensors used in our data collection efforts were the Thies Clima Ultrasonic 3-D Anemometer (THIES) and the BCDVP outfitted with an additional camera and laser. Both of these sensors are designed to resolve small scale turbulent velocities embedded in flow fields.

Figure 17.   Sensors Network Setup
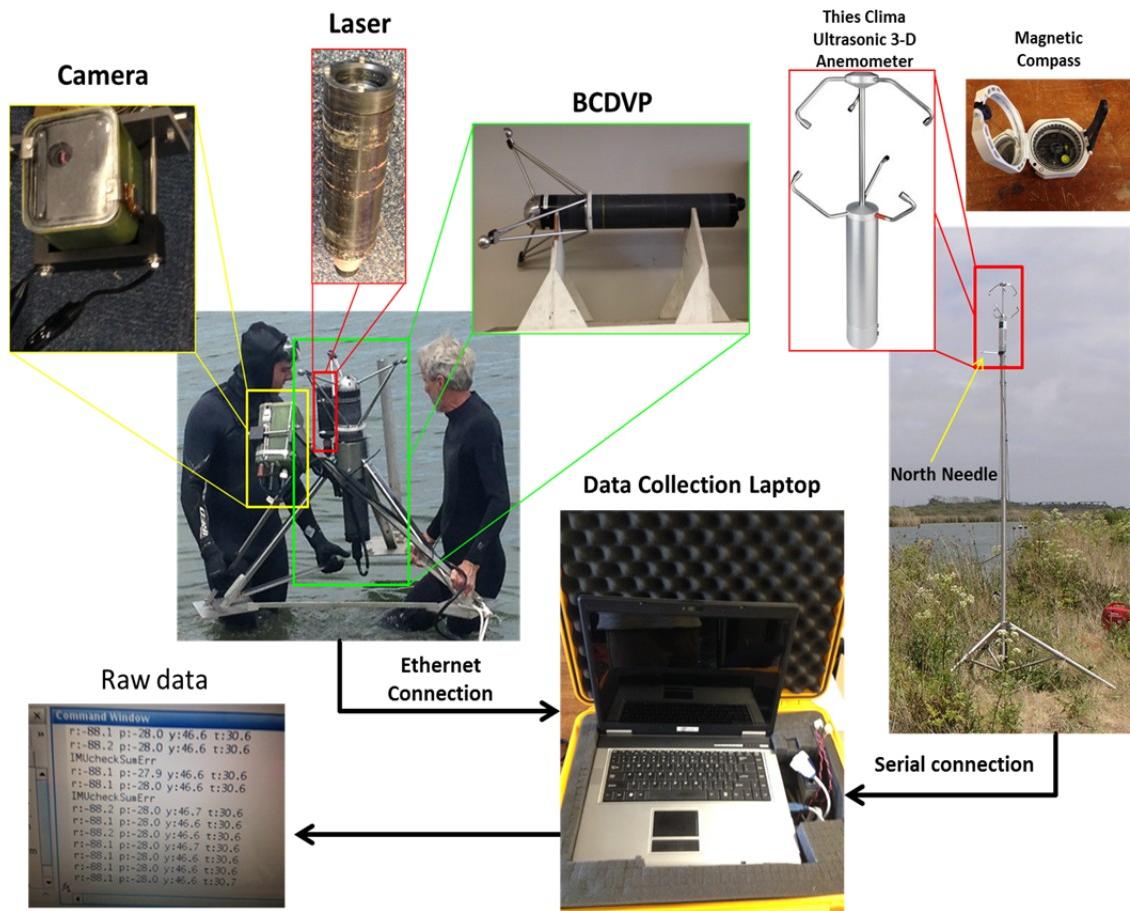
The sensor network diagram shows the components of the various systems used to conduct the experiment and their relation to raw data output. Source: Thies Clima Corporation. Ultrasonic Anemometer 3D. Accessed on Oct 7, 2015. [Available online at:http://www.thiesclima.com/ultrasonic_anemometer_3d_e.html].

Figure 18.   Sensor Deployment Locations
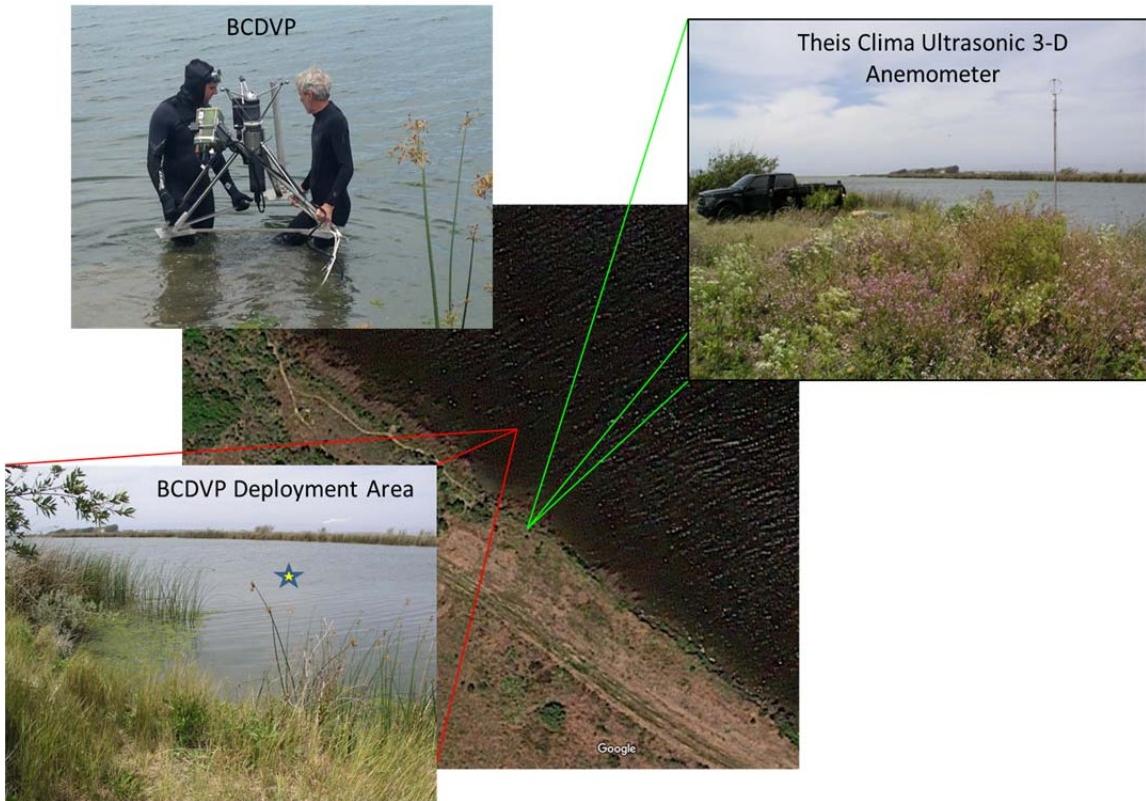
The THIES was deployed on the shore 1.02 m from the waterline on the bank. The BCDVP was deployed 14.25 m from shore in approximately 1.6 meters of water. The BCDVP deployment location is denoted by the ⭐. Map created in Google Earth, October 12, 2015, http://www.google.com/earth/.

A.   THIES CLIMA ULTRASONIC 3-D ANEMOMETER

The THIES measures the 3D wind velocity at a 100 Hz sample rate across an approximate 0.3 m sample volume oriented to magnetic north using a magnetic compass and a pointer attached to the support tower shown in Figure 17. To transfer from degrees magnetic to true north a declination for the area of 13.42′ E was applied.

The three component wind field data is collected by the THIES using three pairs of ultrasonic probes and transferred to the laptop via a serial connection at a 57600 baud rate. The THIES was set up on the bank of the Salinas River at a horizontal distance of 1.0 meters from edge of river. To minimize the influence the influence of the 0.91 m high river bank on the wind field the THIES was located in a relatively open area and the

support mast was fully extended to 3 meters. The total vertical distance from the waterline to the center of the THIES was 3.91 meters. The THIES was placed approximately 26.25 meters downwind and 15.27 m in the crosswind direction from the BCDVP to attempt to capture an accurate wind field as it passes over the BCDVP (Figure 18). Unfortunately, the predominant wind during the observation period aligned dominantly with the river bank. As a result, the upwind brush and other foliage and steep river bank strongly influenced the wind stress by and will be explained further in the discussion section. During the experiment on June 3, 2015, the THIES was set up and operated collecting data over a period of approximately 2 hours and 40 minutes concurrently with the BCDVP (Figure 17). The system was powered by a small generator and transferred the raw data collected by the ultrasonic probes to the laptop via a serial connection. Upon completion the raw data was transferred and analyzed using software written in MATLAB. Further discussion on the analysis of the THIES data collected will be covered in the data analysis section.

B.   BISTATIC COHERENT ACOUSTIC DOPPLER VELOCITY PROFILER

The Bistatic Coherent Acoustic Doppler Velocity Profiler (BCDVP) is the key sensor used for this experiment and an earlier version was previously used in CBLAST experiments at Martha's Vineyard. Using a bistatic transducer configuration, the BCDVP has the ability to sample 3D velocity profiles with 2–3cm diameter by 1cm high sample volumes over a 1.2m range above the instrument. Coherent processing allows the Doppler velocities to be logged at up to 40Hz. During this data collection effort, the BCDVP collected data at a sample frequency of 18.974 Hz resulting in a 0.0527s period between samples. The center beam is vertical while each of the three outer transducers is separated by 120 degrees. The BCDVP's configuration provides a much small effective sample volume than commercially available Janus-configuration ADCP's. The orientation of the system described by Figure 19 allows for the arrangement of the system in an upwind-downwind direction by aligning the wind axis with transducer 1.

The BCDVP was mounted to a tripod raising the transmitter transducer of the sensor to a height 0.84 meters above the sea bed. This meant the maximum effective

37

depth to measure the below wave crest-trough region would be 1.84 meters. A survey of the deployment site (Figure 18) yielded an area with a near flat bottom and approximately 1.6 meter depth. The bed at the deployment location (Figure 18) was composed of a very fine mud. As a result a 0.2 meter buffer for maximum deployable depth was used to avoid deploying the BCDVP in an area where sinking could potentially put the top bin out of range of the surface. A bubble level and an extendable leg were used during the deployment to ensure the system was stable and level along the bottom.

The Doppler processing electronics for each transducer uses 14 bit analog to digital converter to digitize the 1.2 MHz acoustic frequency from the four transducers, and digitally down-convert the received frequencies to baseband, where they are processed by digital signal processors to produce Doppler frequency measurements from each transducer channel at 40 Hz. The data stream is transferred from the BCDVP to the data collection laptop via an Ethernet connection. Linux data logging software running on a lap top computer breaks up the time-tagged data stream 2-hour time-tagged files.

Both the THIES and BCDVP required power from a small generator fed through a power supply to provide the correct DC voltage to each of these systems. The BCDVP was supplemented by a fixed camera and laser (Figure 17) used to illuminate and capture bubble and particle patterns in the water column above it. On the June 3, 2015, deployment, there was minimal suspended sediment and particles as seen in the backscatter data (Figure 20) that would enable the camera and laser to produce usable data. This low particulate load in the water column meant that reflective reverberation of the ensonifying transducer pulses caused by reflections off the bottom and surface caused levels of unusable velocity data within the profile, as shown by the bands highlighted in Figure 20. The reflective reverberation limited the useable bins of the data set to bins 58–74 which represents the surface layer down to 0.16 m. Fortunately, the amount of interference from drifting objects such as algae and sea grass were minimal in this depth range. This surface layer will be the focus area for any BCDVP data analysis.

Figure 19.   BCDVP Probe Diagram
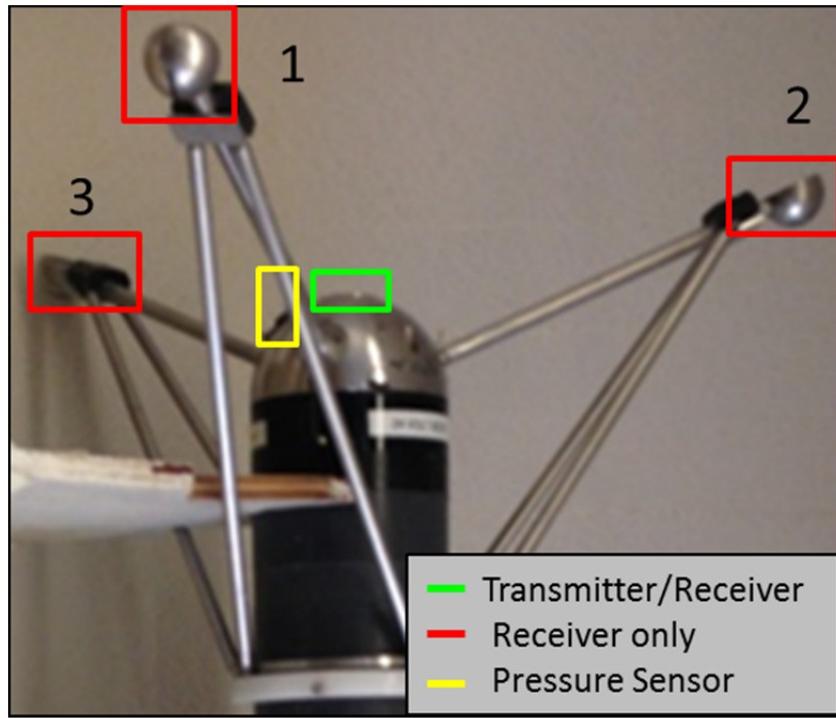
The numbers identify to the probes to set up a reference frame for orientation purposes where transducer 1 is aligned with the instrument coordinate system's y-axis. The system is made up of three transducer arms spaced 120° apart with receivers, a transmitter/receiver, and a pressure sensor as indicated.

Figure 20.   Acoustic Backscatter Power Profile Time Series
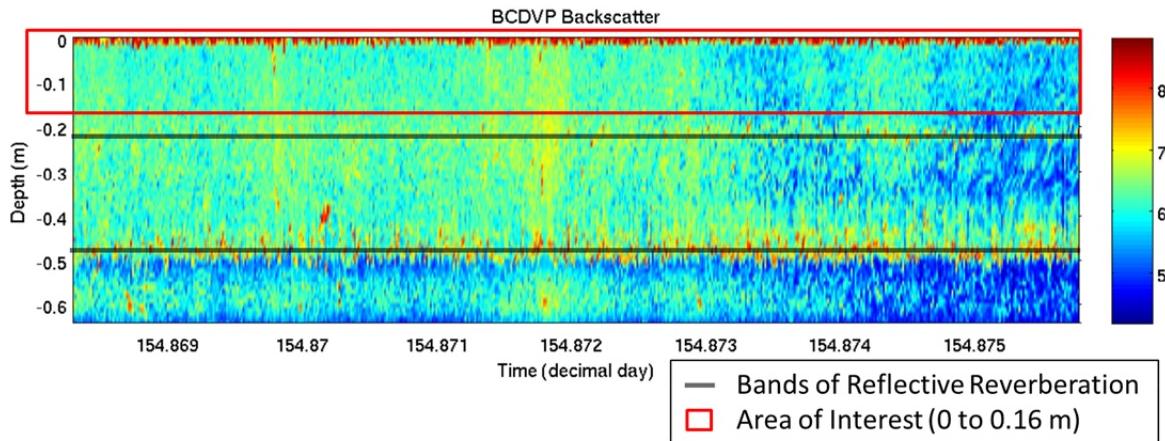
A plot of the BCDVP backscatter data across the period of the data subset highlighting the bands of reflective reverberation and identifying the depths of focus for this data analysis. The logarithmic scale indicates the strength of the return where nine is the strongest and four represents a medium nearly free of scatterers.

THIS PAGE INTENTIONALLY LEFT BLANK

IV. RESULTS

On June 3, 2015, the BCDVP and THIES were deployed at the Salinas River site (Figure 18) recording approximately 2 hours and 40 minutes of data. Of the data collected, only about 10 minutes of it yielded usable results, as wind forcing dropped significantly soon after the instrument deployment. With wind speeds sustained around 6 m s^{-1} from 309° T (Figure 21) the forcing across the surface limited the range of turbulence that could be observed. The limited fetch wave heights associated with the low observed winds did not allow large enough waves to be generated to resolve the surface elevation (η) from either the surface return backscatter or the 1m deep pressure transducer. The low wind speed and low fetch also did not allow wave breaking to occur. The TDM and LWT calculations rely heavily on resolvable η to be able to separate out the various components of motion. Based on the low wind forcing conditions experienced on June 3, 2015, a smaller subset of analysis tools than discussed in section 2 were applicable to this data set. The poor conditions were a result of a spring/summer season characterized by unusually low magnitude sea breeze events, greatly limiting the capture of a strong wind0forced data set. As a result poor conditions and the influence of the previously discussed reflective reverberation bands the ability for in-depth analysis of the main objectives is greatly limited. Therefore, a set of modified objectives were developed. First, determine the wave energy decay with depth and use it to confirm the value of the dominant wavenumber (k). Second, the observed wind stress was compared to stresses within the upper water column, immediately below the waves. Lastly, the presence and characteristics of Langmuir circulations was investigated and compared with previous observations.

Using the high spatial resolution data of the BCDVP a verification of the wave energy decay with depth was made using the vertical profile of the vertical velocity power spectrum. This decay rate was compared with the power spectral peak frequency Shown in the left panel of Figure 22, which was identified as 1.4 Hz. Using linear wave theory, the spectral peak estimated wavelength was 0.78 m, corresponding to a wavenumber of 8.0 m^-1. It is important to note that the calculated wavelength not only

identifies the observed waves as surface gravity waves, but when compared with depth, were found to be deep water waves. Based on linear wave theory for these surface gravity waves the expected decay with depth should follow an e^{-kz} trend. Using a logarithmic plot, Figure 22 the fit line shown here clearly illustrates a fairly consistent fit with the -kz relation for the observed data. The average deviation from the fit line was approximately 0.05 and the largest deviation was found just below the surface with a magnitude of approximately 0.25 m s^{-1}.

Figure 21.　Wind Flow at the Salinas River on June 3, 2015
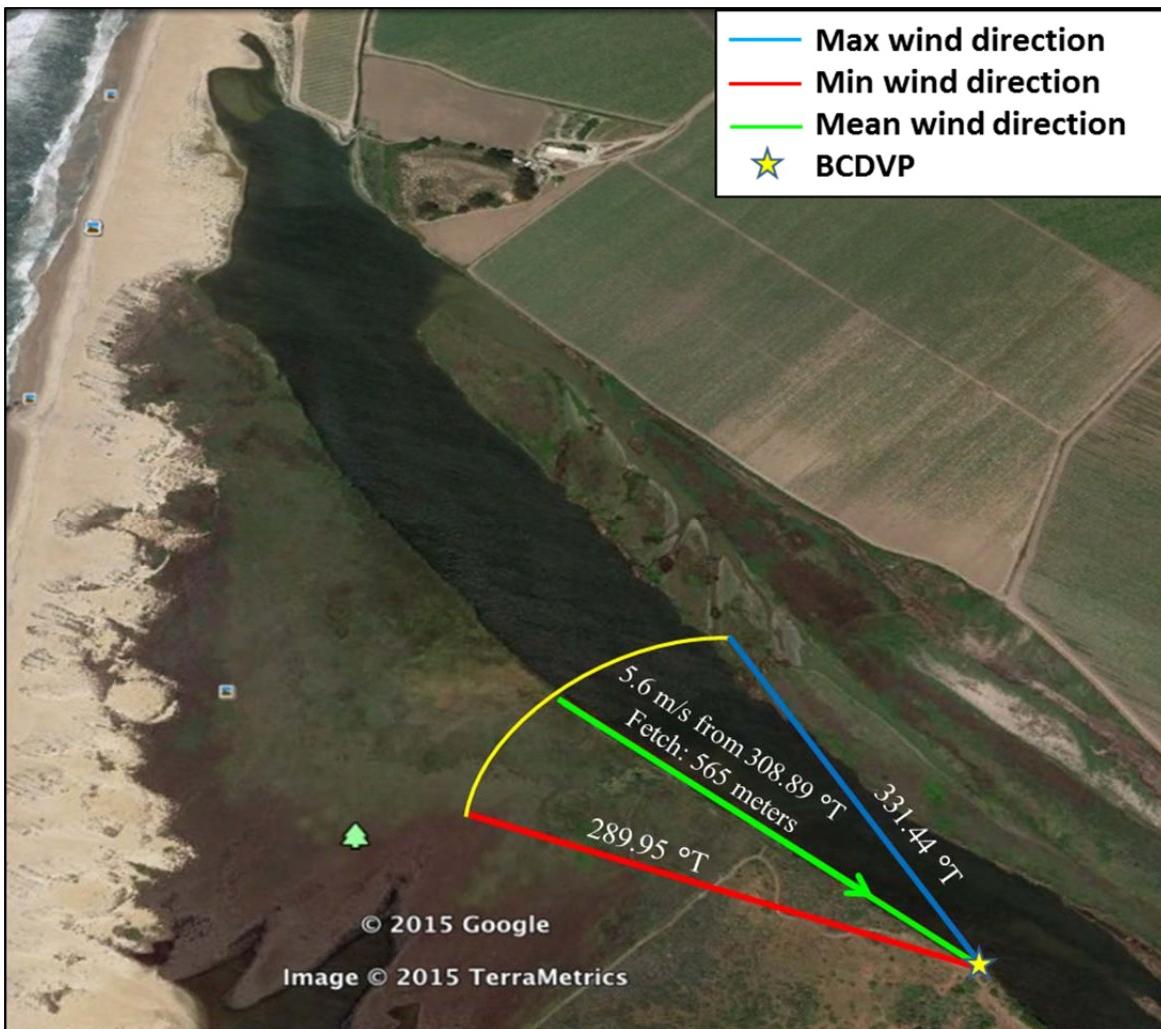
Winds were predominantly from the northwest as expected based on the characteristic sea breeze of this area. The winds shifted towards the west-northwest direction by the end of the observation period as the sea breeze became more coast perpendicular. Map created in Google Earth, November 5, 2015, http://www.google.com/earth/.

Figure 22.   Decay of Wave Orbital Velocity with Depth
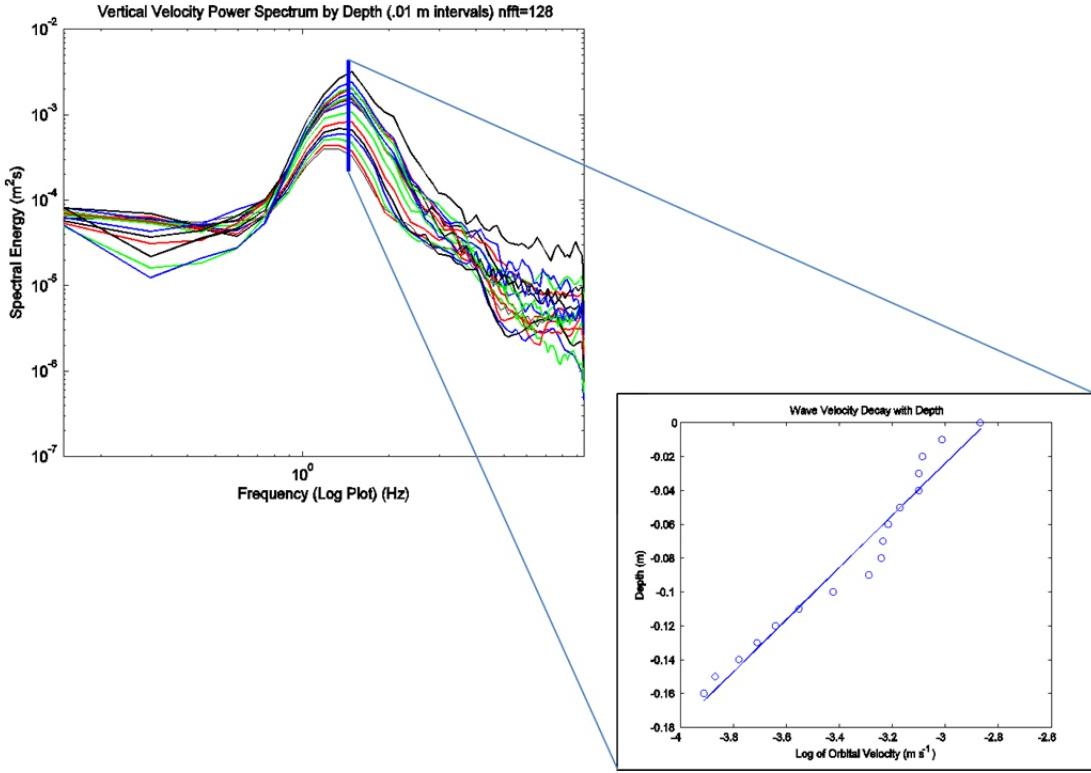
Using the power spectrum for the vertical velocity the decay with depth shows the spectral peak corresponding to the wave energy occurs around 1.14 Hz and the wave velocity decay with depth shows a good fit as expected based on LWT. Each spectrum color represents a different depth decreasing by 0.01 m down to 0.16 m. The blue line indicates the location of peak energy for each spectrum as depth decreases. The fit line in this logarithmic plot defining the -kz relation associated with the wave velocity decay with depth.

For the remainder of this analysis, the focus will be on a data subset from yearday 154.8683 to 154.8758 that translates to approximately 10 minutes of data. An initial look at the wind field data collected by the THIES (Figure 26) illustrates minimal variability in the wind direction and forcing for this period. However, analysis of the wind stress showed a significant difference between the wind stresses derived from a direct eddy-correlation stress calculation from the 100 Hz THIES data and the values found using a bulk formula method. First, a direct calculation of the total wind stress (τ) was conducted by expanding Equation 1.15 to include the cross-wind stress component $\overline{v'w'}$,

$$\tau = \rho_{air} * \sqrt{\overline{u'w'}^2 + \overline{v'w'}^2} \, , \tag{1.26}$$

where $\rho_{air} = 1.23 \frac{kg}{m^3}$ is the density of air, $\overline{u'w'}$ and $\overline{v'w'}$ are the covariances (Gerbi et al.

2008). The direct calculation yielded values with a mean wind stress of 0.430 N m^{-2} (Figure 25). Next, the bulk formula method was carried out using the equation

$$\tau = \rho_{air} C_d U^2 ,$$ (1.27)

where $\rho_{air} = 1.23 \frac{kg}{m^3}$ is the density of air, U is the wind speed and $C_d = 0.0018$ is the drag coefficient (Smith 1988). The drag coefficient was derived from the curves in Figure 23 using the mean observed wind (5.6 m s^{-1}) and estimated open water fetch (565 m). The drag coefficient curves (Figure 23) are based on fetch (x) and fetch limited wave growth function (x_*) as a function of wind speed. The fetch limited wave growth function (x_*) (Figure 23) is calculated using

$$x_* = \frac{xg}{U^2}$$ (1.28)

where U is the wind speed (m s^{-1}) and g is the acceleration due to gravity ($g = 9.8 \, m/s^2$), and x is the fetch (Hwang 2005).

Figure 23. Drag Coefficient Curves

x = 565 m

x∗ = 176.56

Fetch

$C_d = 0.0018$
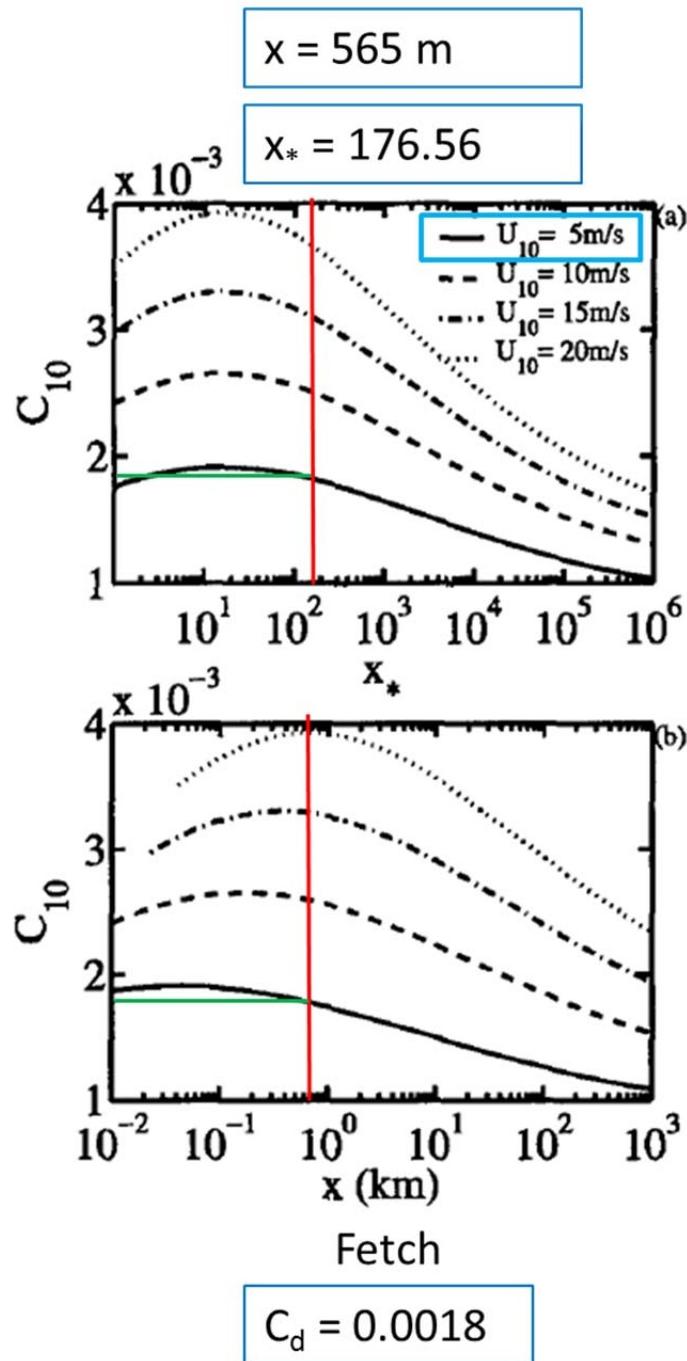
Drag coefficient curves based on fetch (x) and fetch limited wave growth function (x_*) based on mean wind speed and fetch. Based on the observed average wind speed of 5.6 m s^{-1} and using the fetch x = 565 m (Figure21), a C_d value of 0.0018 was found. Source: Hwang, P. A., 2005: Temporal and spatial variation of the drag coefficient of a developing sea under steady wind forcing, *J. Geophys. Res.*, **110**, C07024, doi:10.1029/2005JC002912.

45

Using the bulk formula method resulted in a mean wind stress value of 0.0718 N m-2 (Figure 25 and 26). The variation between the two values is on the order of six times greater for the directly calculated wind stress Figure 25. To further investigate a second look at the upwind path was conducted focusing on its relation to the river bank and any potential obstructions. Figure 24 shows a height cross section of the river bank highlighting the downwind and upwind views from the THIES deployment site. With the wind nearly parallel to the shoreline and the THIES's deployment location 1.02 m inland from the waterline it became clear that the influence upwind of the upstream vegetation a strong effect on turbulence levels, and the resulting surface tresses of the wind field. Though the tall vegetation in the upwind direction and the truck were greater than 20 meters away from the THIES (Figure 24), the predominant wind direction was aligned with the bank and therefore captured more of the overland wind stress field rather than providing an accurate estimate of the open water wind stress field over the BCVDP deployment site. The bulk formula method was chosen to estimate the surface stresses over the BCDV. Using the bulk wind stress values shown in Figure 26, the observed values were found to be on average slightly less than those found over the open ocean by both Weller and Price (1988) (Figure 8) and the 0.10 N m^{-2} seen by Gargett and Wells (2007) as expected for the very small amplitude wind waves associated with the fetch and mean wind speed for the Salinas River data set.

Figure 24.   Salinas River Upwind Cross Section
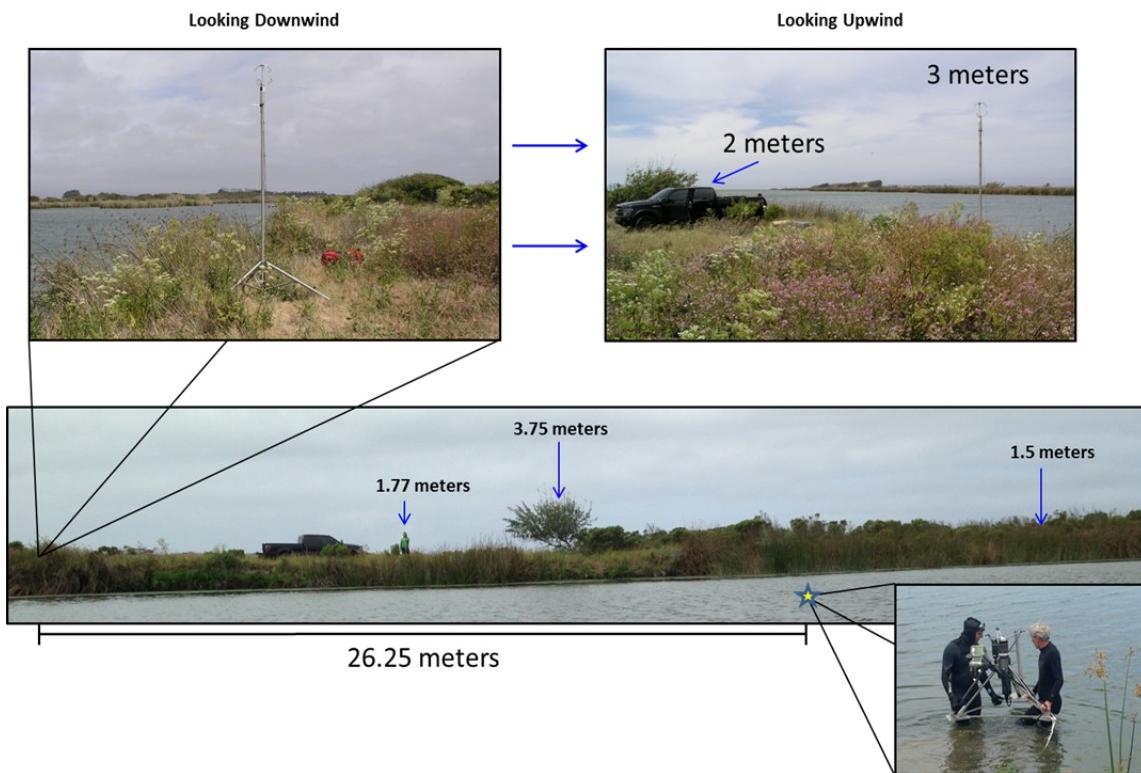
A look at a cross section of the Salinas River bank where the THIES was deployed, note the heights of various obstructions upwind that contributed to a higher drag coefficient and therefore a higher wind stress. The shoreline parallel distance (26.25 m) between the BCDVP and the THIES is shown.

Figure 25.   Eddy Correlation Wind Stress versus Bulk Formula
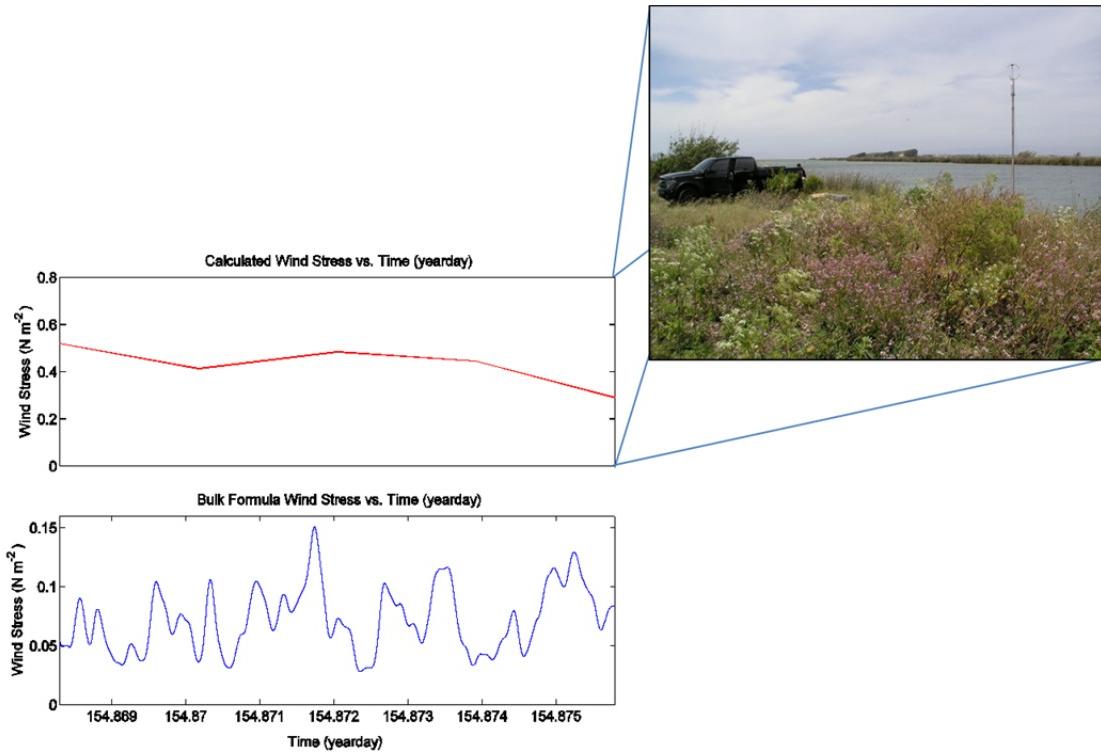
A clear depiction of the influence of vegetation and topography on the wind stress values. For this reason the wind stress will call upon the bulk formula method for this data analysis. Note the calculated wind stress is a series of 2 minute averages across the data subset to clearly show the magnitude difference between the two plots.

Subsurface stresses and friction velocities were calculated to allow for a comparison of stresses across the air-sea boundary. First, to aid in this Figure 26 provides a summary of all the above surface components including the bulk formula derived wind stresses, wind direction, wind speed, and the current velocity data. Next, to derive the values for the friction velocity (u*), an expanded version of Equation 1.11 is used to account for the $\overline{v'w'}$ crosswind stress component yielding the equation

$$u* = (\overline{u'w'}^2 + \overline{v'w'}^2)^{.25},$$
(1.29)

where $\overline{u'w'}$ and $\overline{v'w'}$ are the ensemble averaged covariances of the horizontal velocity fluctuating components and vertical velocity fluctuations. The subsurface stress profiles were created using Equation 1.26 substituting rho air for rho water (Figure 27). The calculated values (Figure 27) show a fairly uniform momentum flux is occurring in the

48

near surface layer, with mean stress values of 0.09 N m^{-2} close to the estimated wind surface stress value of 0.072 N m^{-2}. It is important to note the presence of an anomaly highlighted by the red box in Figure 27. The cause of this rapid increase in the friction velocity and stress values is not known. It is possible that this increase at 0.1 m depth is the result of Langmuir circulations that have cell velocity maxima near this depth. From the water column stress profile in Figure 27, a comparison to the above surface wind stress estimate shown in Figure 26 yields a mean wind stress value of 0.072 N m^{-2} and a mean water column stress value of 0.075 N m^{-2}, a close agreement of momentum transfer across the boundary. The difference between the bulk parameterized wind stress and the stresses in the water column is well within the error bounds of the bulk wind stress estimates. Additionally, a small stress deficit is expected in the bulk stress estimate as a result of local wind wave generation. The high vertical resolution BCDVP observations allow the structure of the low frequency turbulent motions to be investigated.

Figure 26.   Time Series of Wind Data and Current Speed Profile
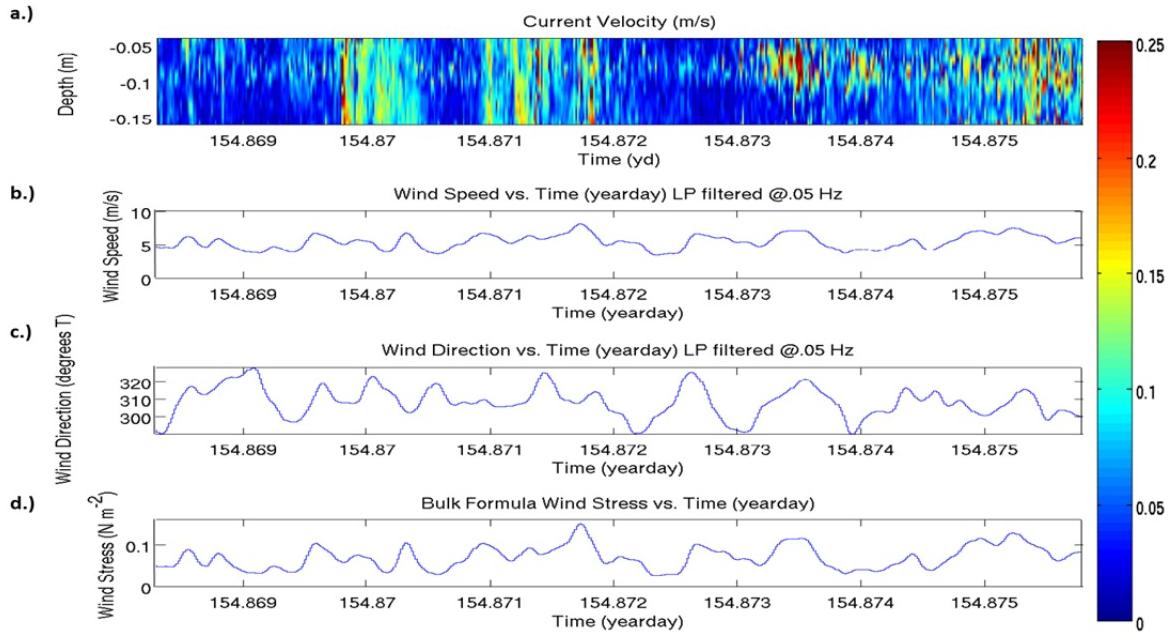
The time series for the data subset showing: a) current speed (color bar indicates flow in meters per second), b) wind speed, c) wind direction, and d) calculated wind stress using the bulk formula based on a C$_d$ of 0.0018. The mean wind speed is 5.6 m s^{-1} (b), the mean wind direction is 308.9˚T (c) and the mean wind stress is 0.0718N m^{-2} (d). Positive current speed is in the downwind direction.

49

Figure 27.　Friction Velocity and Stress
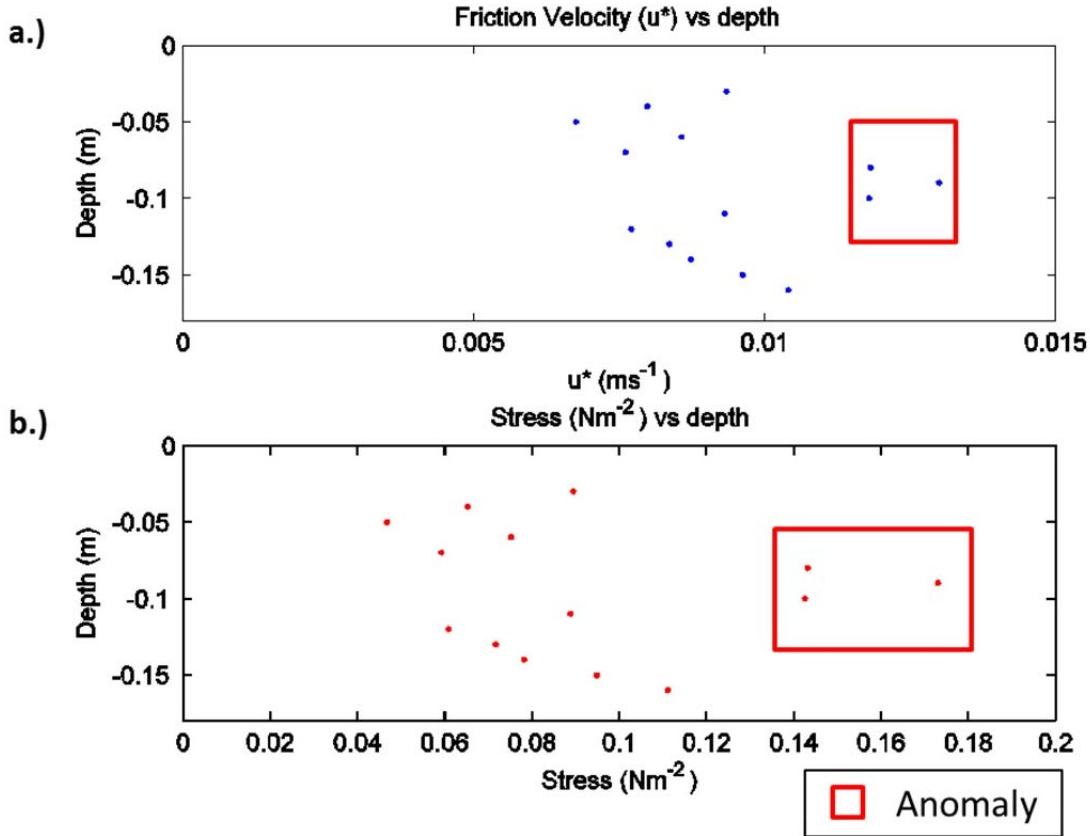
a) Friction velocity u* and b) stress values align well with the findings by Weller and Price (1988) shown in Figure 8. The expected momentum decay with depth is not fully captured here as only a 0.17 m depth range yielded usable data. Note the anomaly in the data subset for which the cause is unknown.

The period selected for analysis coincides with relatively stronger winds along the river yielding the greatest fetch and strongest wind forcing for the observed conditions on June 3, 2015. To help identify key structures associated with Langmuir circulation such as the presence of a downwind jet, upwelling, and downwelling patterns, the BCDV 3D current vector profile coordinate system was rotated to align with the mean wind direction. Additionally, this facilitates a comparison of the wind forcing with the upper ocean current profiles. Figure 28 shows the results of this rotation and shows a strongly sheared, weak downwind current flow and relatively large crosswind flow.

Figure 28.   Mean Component Velocities after Coordinate Rotation
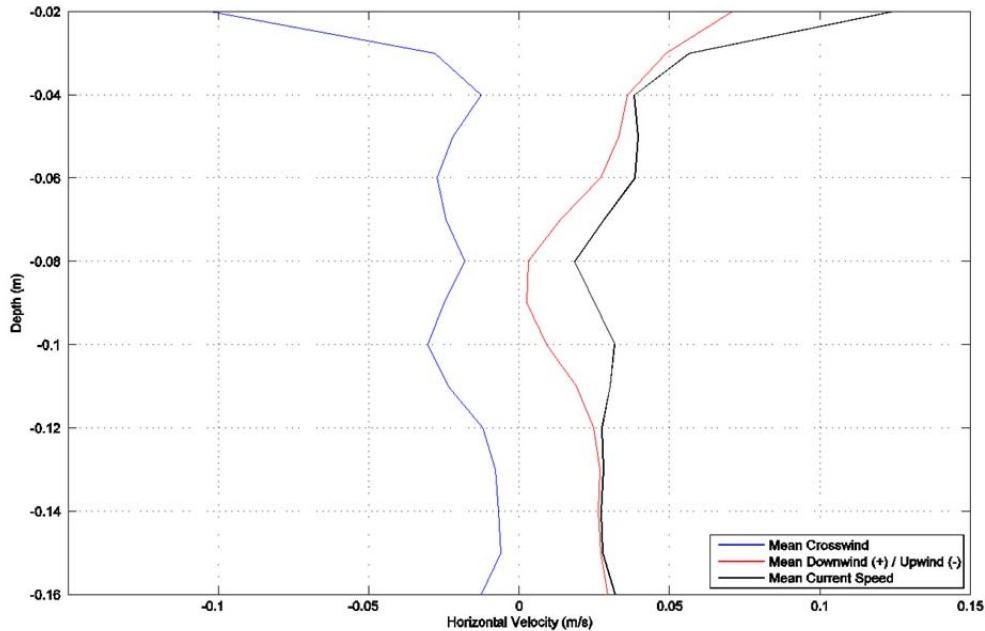
The mean velocities across the depths of interest shown in Figure 20 after the rotation of the coordinate system of the instrument to orient the +v component in the downwind direction. The trend shows a decay in surface current velocity with depth as expected.

To quantify the presence of Langmuir cells, a 2 minute section of the BCDVP velocity profile time series is used. It is important to note that the current velocity profile derived from the horizontal components of the BCDVP data identifies the dominant near-surface mean flow to be in the downwind direction (Figure 26 and 28). As previously discussed, weak wind forcing, negligible wave breaking, and the lack of suspended scatterers present during the period of observation limited the use of the BCDVP backscatter data to identify features of the Langmuir circulation cells. As a result the backscatter profile was unable to provide any quantifiable evidence that captured the transport of bottom sediment, surface particles, or bubbles typically associated with Langmuir circulations in shallow water. This prevented any comparison with the previously discussed findings of Marimorino et al. (2005) and Gargett and Wells (2007) regarding sediment transport associated with Langmuir circulations.

Horizontal velocity time series seen in Figure 29 identify areas of upwelling and downwelling in addition to the vertical, downwind/upwind, and crosswind velocities. The magnitudes of the vertical velocities associated with the down welling, ~0.04 m s^{-1}, are significantly greater than the ~0.020 m s^{-1} velocities associated with the areas of upwelling. The presence of a downwind jet is readily apparent in Figure 29 and is highlighted by a black polygon. As described by Wilczak and Tillman (1980), the downwind jet is located in the area of convergence between two successive downwelling cells and is characterized by a region of much stronger flow in the downwind direction as illustrated in Figure 6.

The time scale of the observed Langmuir event described in Figure 29 was on the order of approximately 85 s. Since the Langmuir cells were advecting in the crosswind direction at a rate of approximately 0.1 m s^{-1} derived from the crosswind velocity profile (Figure 29b), the length scale for the upwelling and downwelling parts of the cell highlighted by the green and red boxes in Figure 29 reflect a horizontal width associated with downwelling (~ 1.5 m) to be smaller than the upwelling region (~ 2.4 m). This is consistent with the previously discussed results of Weller and Price (1988) (Figure 6) and Gargett and Wells (2007), that show the downwelling portion being stronger and narrower than the wider and weaker regions of upwelling.

Despite the small scale of this Langmuir event, a peak was presented in the power spectrum of vertical velocity (Figure 30) in the low frequency energy containing portion of the energy density spectrum typically associated with Langmuir circulation. The energy associated with Langmuir circulation tends to remain fairly constant down from the surface and increased slightly increases with depth, consistent with the influence of the downwelling and upwelling parts of the cells advecting past the BCDV.

Figure 29.   BCDVP Velocity Data
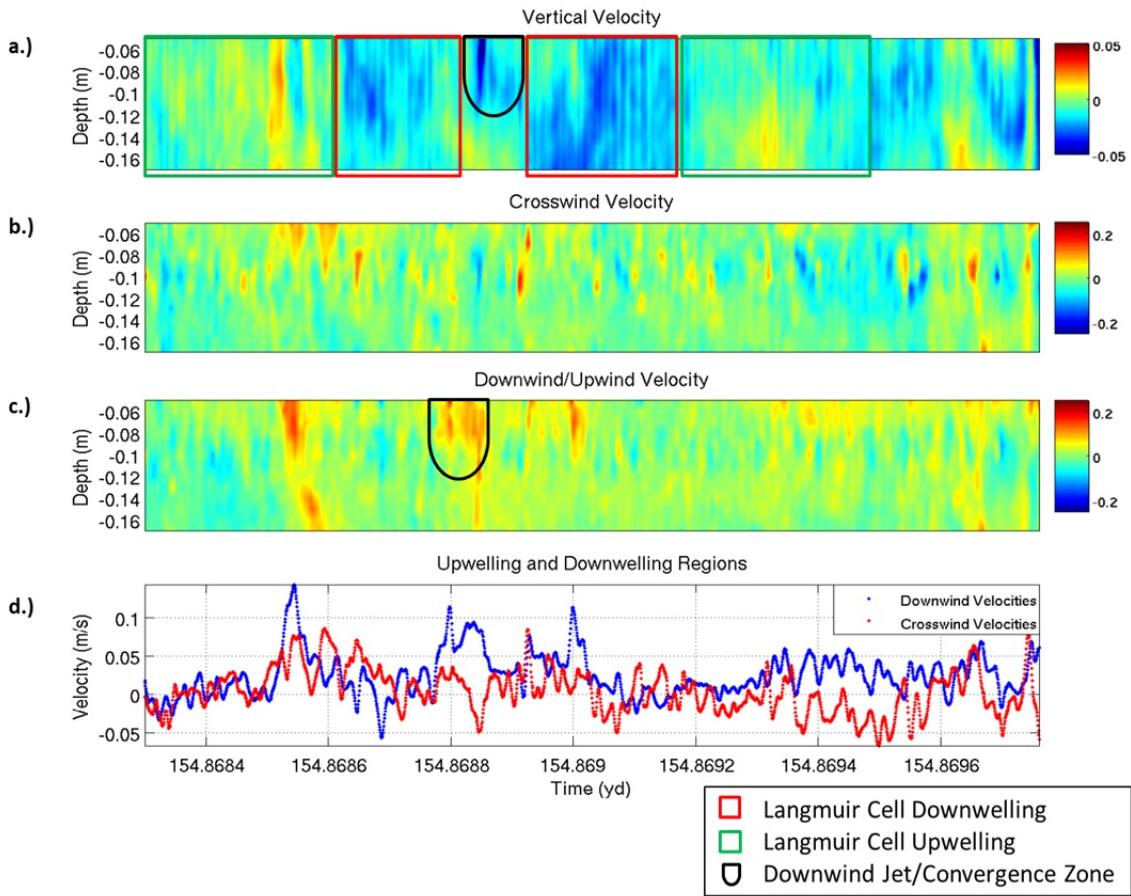
Time series graph of a 2-minute snippet of BCDVP data displaying a) vertical velocity, b) crosswind velocity, c) downwind/upwind velocity, and d) upwelling and downwelling regions. Evidence shown of Langmuir cells based on the regions of upwelling, downwelling, and the downwind jet located in the convergence zone recalling Figure 6. Color bar shows flow in meters per second where positive is upward (a), downwind (b) or crosswind to the right of the downwind flow (c).

Figure 30.   Wave Energy and Langmuir Energy
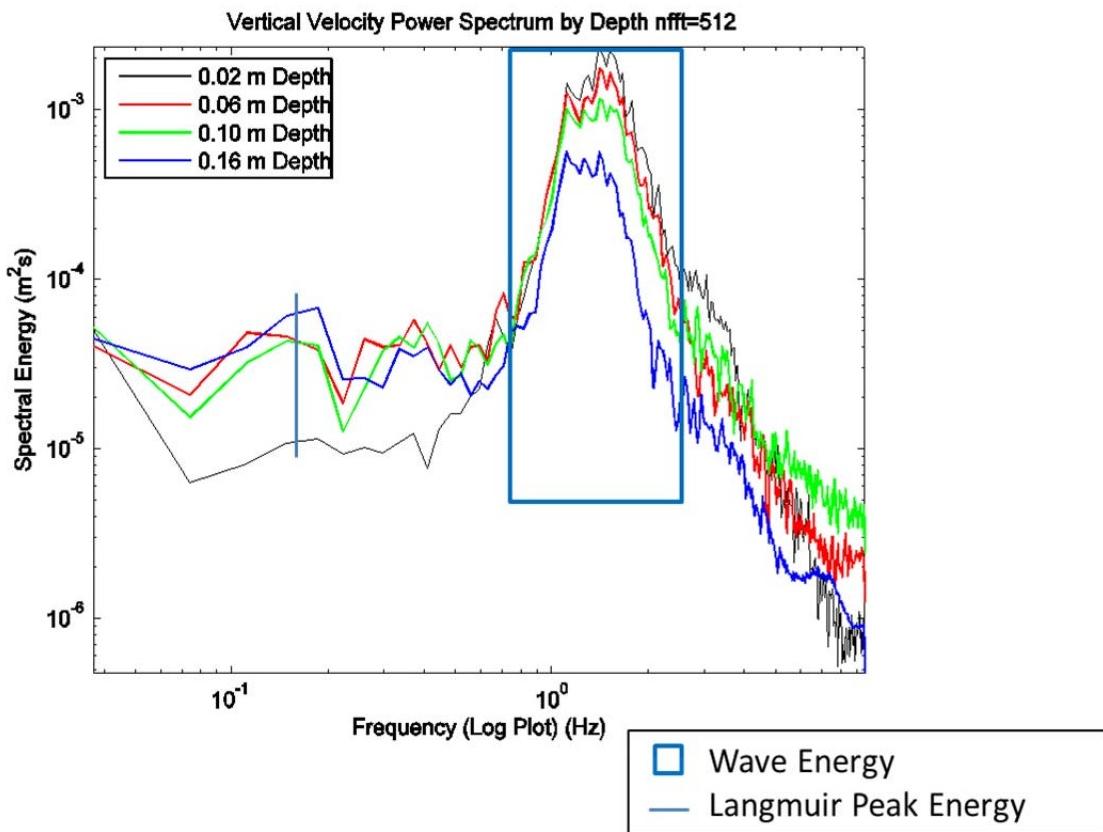
The spectrum shows the peak wave energy focused around 1.1 Hz and the Langmuir energy peak focused around 0.15 Hz.

V. SUMMARY AND FUTURE RESEARCH

A. SUMMARY

In an effort to further understand the role of Langmuir circulation and wave breaking, a set of instruments were deployed to measure surface wind forcing and the detailed upper ocean response in a short fetch coastal location. The data subset collected at the Salinas River on June 3, 2015, identified key turbulent energy containing features such as Langmuir circulations. Limited by less than climatological wind conditions the initial objective to make very high spatial resolution profile measurements of the 3-D velocity field right up to the crest-trough region of wind-forced surface gravity waves, and study the low frequency turbulent motions below the waves needed to be modified. Therefore, the following three modified objectives were developed and met. First, an analysis of the wave velocity decay with depth confirmed the wavenumbers (k) depth (z) relation with the observed data yielding a near fit to the -kz plotted line in logarithmic space (Figure 22). Second, the observed eddy correlation wind stress and estimated wind stress using a bulk formula identified a large departure from the expected values for these wind-fetch conditions. This identified a larger drag coefficient (Figure 25) caused was by vegetation and other obstructions in the upwind path of the wind turbulence sensor since the winds were nearly parallel to the bank (Figures 21 and 24) and the wind sensor was inshore from the ocean profile instrumentation. Lastly the presence of Langmuir circulations were confirmed, and their temporal and spatial scales were quantified The downwind jet, scale of downwelling and upwelling cells, peak energy values, and overall scale of a Langmuir event were estimated for the data subset (Figures 29 and 30). The Langmuir events identified in this analysis meet the five criteria described by Gargett and Wells (2007), and were readily apparent during the data analysis. The location of the Langmuir circulation peak energy (Figure 30) within the turbulent containing portion of the vertical velocity frequency spectrum indicates their role in contributing to the turbulent stresses within the water column. The very high spatial resolution of the BCDVP was capable of capturing the small scale Langmuir event seen in Figure 29. This provides a future opportunity to investigate in depth the processes associated with small

scale circulations such as this one and the ones described by Gargett and Wells (2007) (Figure 10). Despite the limited data set for this thesis, the high resolution data provided by the BCDVP still enabled the turbulent structure below wind forced surface gravity waves to be resolved and analyzed.

Despite the BCDVP's and THIES's ability to produce high resolution data capable of resolving wave and turbulent processes, , the environmental conditions present during this experiment were not sufficient enough to produce data capable of supporting any new findings. Given the limited fetch required for this research, the absence of the higher wind velocities typically experienced during the summer sea breeze events resulted in only a marginal data set. It is important to note that the data did identify and confirm the presence of key structures associated with momentum transfer and Langmuir circulations. The findings discussed in this thesis shows the need for future field research and is an indicator as to how effective it could be at improving model parameterization of momentum transfer processes across the air-sea boundary especially those associated with wind driven processes.

B. FUTURE RESEARCH

The non-tidal and non-swell affected Salinas River can still serve as a useful location to study turbulence associated with wind generated surface gravity waves but it must be during a during higher wind event and a time where it is free of algae. To effectively employ these systems in order to further the research of turbulence associated with surface gravity waves a site with sufficient wind forcing (> 10 m s^{-1}) across a sufficient fetch (>1 km) free from obstructions such as surface algae, bordering topography, and vegetation is required. The ability to conduct repeat measurements is important to ensure the data collected is of sufficient length to cover a range of conditions including strong forcing spanning 10 m s^{-1} to ensure saturated wave breaking conditions. An important addition to the BCDVP and THIES sensors would be temperature and salinity measurements below the surface to reveal water column stratification under light wind forcing conditions. Additionally, the THIES needs to be deployed over the water in a manner that limits the influence of topography and vegetation, preferably just

downwind of the BCDV profile location. Additionally, the utilization of the BCDVP may be more effective deployed in deeper water using an arm system to limit the bottom generated reflective reverberation effects seen in the data. Ideally the arm system would originate from below to limit its effects on the flow field.

With some of the improved methods described in this thesis, future research could produce a large usable data set capable of meeting the CBLAST goal of providing "the detailed analysis of closure models across air-sea interface and their potential use in further assisting with identifying turbulent motions generated by both micro-breaking and full breaking waves in the presence of surface gravity waves" (Edson et al. 2007).

THIS PAGE INTENTIONALLY LEFT BLANK

LIST OF REFERENCES

Benilov, A. Y., and B. N. Filyushkin, 1970: Applications of the linear filtration methods to the fluctuation analysis in the sea upper layer, *Izv. Acad. Sci. USSR Atmos. Oceanic Phys., Engl. Transl.*, **6**(8), 477–482.

Benilov, A. Y., O. A. Kuznetsov, and G. N. Panin, 1974: On the analysis of wind wave-induced disturbances in the atmospheric turbulent surface layer. *Bound.-Layer Meteor.,* **6,** 269–285.

Dean, R. G., 1965: Stream function representation of nonlinear ocean waves, *J. Geophys. Res.,* 7018, 4561–4572.

Edson J., T. Crawford, J. Crescenti, T. Farrar, J. French, et al. 2007: The coupled boundary layers and air-sea transfer experiment in low winds (CBLAST-Low). *Bull. Am. Meteorol. Soc.* **88**,342–56

Flierl, G. and R. Ferrari, 2007: *12.820 Turbulence in the Ocean and Atmosphere, Spring 2007.* Massachusetts Institute of Technology: MIT OpenCourseWare, Accessed Sep 29, 2015. [Available online at: http://ocw.mit.edu]

Gargett, A., and J. R.Wells, 2007: Langmuir turbulence in shallow water. Part 1. Observations. *J. Fluid Mech.,* **576**, 27–61

Gerbi, G. P., J. H. Trowbridge, J. B. Edson, A. J. Plueddemann, E. A. Terray, and J. J. Fredericks, 2008: Measurements of momentum and heat transfer across the air–sea interface. *J. Phys. Oceanogr.*, **38**, 1054–1072.

Google, 2015: Google Earth. Accessed on Oct 12, 2015, [Available online at: http://www.google.com/earth/]

Govender, K., G. P. Mocke, and M. J. Alport, 2004: Dissipation of isotropic turbulence and length-scale measurements through the wave roller in laboratory spilling waves. *J. Geophys Res.*, **109,** C08018, doi:10.1029/2003JC002233.

Guza, R. T., and E. B. Thornton, March 1980: Local and Shoaled Comparisons of Sea Surface Elevations, Pressures and Velocities. *J. Geophys Res.*, **85:C3**, 1524–1530.

Hinze, J. O., 1975: *Turbulence*, 2nd ed., McGraw-Hill.

Hossain, N., 2012: Turbulence Modeling. *Computational Mechanics.* Accessed Sep 01, 2015. [Available online at: http://naimhossain.blogspot.com/2012/08/turbulence-modeling.html]

Hwang, P. A., 2005: Temporal and spatial variation of the drag coefficient of a developing sea under steady wind forcing, *J. Geophys. Res.*, **110**, C07024, doi:10.1029/2005JC002912.

Jiang, J.-Y., R. L. Street, and S. P. Klotz, 1990: A study of water-turbulence interaction by use of a nonlinear water wave decomposition technique, *J. Geophys. Res.*, **95**, 16037–16054, doi:10.1029/JC095iC09p16037.

Kitaigorodskii, S. A., and J. L. Lumley, 1983: Wave-turbulence interactions in the upper ocean. Part I: The energy balance of the interacting fields of surface wind waves and wind-induced three-dimensional turbulence. *J. Phys. Oceanogr.,* **13,** 1977–1987.

Langmuir, I., 1938: Surface motion of water induced by wind, *Science, 87,* 119–123.

Magnaudet, J., and L. Thais, January 1995: Orbital rotational motion and turbulence below laboratory wind waves. *J. Geophys Res.*, **100**, C1 757–771.

Magnaudet, J., and L. Thais, January 1995: A triple decomposition of fluctuating motion below laboratory wind water waves. *J. Geophys Res.*, **100,** C1 741–755.

McPhee, M. G., 2008: *Air-Ice-Ocean Interaction: Turbulent Ocean Boundary Layer Exchange Processes.* Springer, 215 pp.

Pope, S. B., 2000: *Turbulent Flows*. Cambridge, UK: Cambridge Univ. Press. Accessed Nov 03, 2015. [Available online at: http://www.eng.utah.edu/~mcmurtry/ Turbulence/turblt.pdf]

Smith, S. D., 1988: Coefficients for sea surface wind stress, heat flux, and wind profiles as a function of wind speed and temperature. *J. Geophys Res.,* **93**, 15467-15472.

Stanton, T. P., 2001. A Turbulence-Resolving Coherent Acoustic Sediment Flux ProbeDevice and Method For Using. U.S. Patent 6,262,942, issued 17 July 2001.

Taylor, G. I., 1938: The spectrum of turbulence, *Proc. R. Soc. London Ser. A*, **164**, 476.

Thies Clima Coorporation. Ultrasonic Anemometer 3D. Accessed on Oct 7, 2015. [Available online at: http://www.thiesclima.com/ultrasonic_anemometer_3d _e.html]

Weller, R. A., and J. F Price, 1988: Langmuir circulation within the oceanic mixed layer. *Deep-Sea Res.* **35**: 711–747

Wilczak, James M., and J. E. Tillman, 1980. "The three-dimensional structure of convection in the atmospheric surface layer." *J. Atmos. Sci,*. **37.11**, 2424–2443.

Wilkin, J., and L. Lanerolle, 2005: Ocean forecast and analysis models for coastal observatories. *Ocean Weather Forecasting: An Integrated View of Oceanography,* E. Chassignet and J. Verron, Eds., Springer, 549–572.

INITIAL DISTRIBUTION LIST

1.   Defense Technical Information Center
        Ft. Belvoir, Virginia

2.   Dudley Knox Library
        Naval Postgraduate School
        Monterey, California